JOURNAL OF PETROLOGY | VOLUME 52 | NUMBER 6 | PAGES 1077–1105 | 2011 | doi:10.1093/petrology/egr019

Magma and Volatile Supply to Post-collapse Volcanism and Block Resurgence in Siwi Caldera (Tanna Island, Vanuatu Arc)

N. MÉTRICH[1,2]*, P. ALLARD[1,3], A. AIUPPA[4,5], P. BANI[6], A. BERTAGNINI[2], H. SHINOHARA[7], F. PARELLO[4], A. DI MURO[1], E. GARAEBITI[8], O. BELHADJ[9] AND D. MASSARE[1]

[1]INSTITUT DE PHYSIQUE DU GLOBE, SORBONNE-PARIS CITÉ, UMR 7154 CNRS, UNIVERSITÉ PARIS DIDEROT, F-75005, PARIS, FRANCE

[2]ISTITUTO NAZIONALE DI GEOFISICA E VULCANOLOGIA, SEZIONE DI PISA, 56126, PISA, ITALY

[3]ISTITUTO NAZIONALE DI GEOFISICA E VULCANOLOGIA, SEZIONE DI CATANIA, 95125 CATANIA, ITALY

[4]DISTeM, UNIVERSITÀ DI PALERMO, PALERMO, ITALY

[5]ISTITUTO NAZIONALE DI GEOFISICA E VULCANOLOGIA, SEZIONE DI PALERMO, 90123 PALERMO, ITALY

[6]INSTITUT DE RECHERCHE ET DÉVELOPPEMENT, 98848 NOUMÉA, NEW CALEDONIA, FRANCE

[7]GEOLOGICAL SURVEY OF JAPAN, AIST, TSUKUBA, IBARAKI, 305-8567, JAPAN

[8]DEPARTMENT OF METEOROLOGY AND GEOHAZARDS, PORT VILA, VANUATU

[9]SIS2M, CEA-SACLAY, 91191, GIF SUR YVETTE, FRANCE

RECEIVED SEPTEMBER 15, 2010; ACCEPTED APRIL 13, 2011
ADVANCE ACCESS PUBLICATION JUNE 3, 2011

Siwi caldera, in the Vanuatu arc (Tanna island), is a rare volcanic complex where both persistent eruptive activity (Yasur volcano) and rapid block resurgence (Yenkahe horst) can be investigated simultaneously during a post-caldera stage. Here we provide new constraints on the feeding system of this volcanic complex, based on a detailed study of the petrology, geochemistry and volatile content of Yasur–Siwi bulk-rocks and melt inclusions, combined with measurements of the chemical composition and mass fluxes of Yasur volcanic gases. Major and trace element analyses of Yasur–Siwi volcanic rocks, together with literature data for other volcanic centers, point to a single magmatic series and possibly long-lived feeding of Tanna volcanism by a homogeneous arc basalt. Olivine-hosted melt inclusions show that the parental basaltic magma, which produces basaltic-trachyandesites to trachyandesites by ~50–70% crystal fractionation, is moderately enriched in volatiles (~1 wt % H_2O, 0·1 wt % S and 0·055 wt % Cl). The basaltic-trachyandesite magma, emplaced at between 4–5 km depth and the surface, preserves a high temperature (1107 ± 15°C) and constant H_2O content (~1 wt %) until very shallow depths, where it degasses extensively and crystallizes. These conditions, maintained over the past 1400 years of Yasur activity, require early water loss during basalt differentiation, prevalent open-system degassing, and a relatively high heat flow (~10^9 W). Yasur volcano releases on average ≥ 13·4 × 10^3 tons d^{-1} of H_2O and 680 tons d^{-1} of SO_2, but moderate amounts of CO_2 (840 tons d^{-1}), HCl (165 tons d^{-1}), and HF (23 tons d^{-1}). Combined with melt inclusion data, these gas outputs constrain a bulk magma degassing rate of ~5 × 10^7 m^3 a^{-1}, about a half of which is due to degassing of the basaltic-trachyandesite. We compute that 25 km^3 of this magma have degassed without erupting and have accumulated beneath Siwi caldera over the past 1000 years, which is one order of magnitude larger than the accumulated volume uplift of the Yenkahe resurgent block. Hence, basalt supply and gradual storage of unerupted degassed basaltic-trachyandesite could easily account for (or contribute to) the Yenkahe block resurgence.

*Corresponding author. Present address: Institut de Physique du Globe de Paris, Géologie des Systèmes Volcaniques, Bureau 438, 1, rue Jussieu, 75238, Paris cedex 05, France. E-mail: metrich@ipgp.fr

© The Author 2011. Published by Oxford University Press. All rights reserved. For Permissions, please e-mail: journals.permissions@oup.com

Downloaded from http://petrology.oxfordjournals.org/ by guest on March 22, 2015

KEY WORDS: *Vanuatu arc; Yasur; gas fluxes; volatiles; melt inclusions; resurgent block; volcano thermal budget*

INTRODUCTION

Caldera collapse, produced by massive magma withdrawal during explosive eruptions, corresponds to the culminating stages in the evolution or eruptive cycles of volcanoes beneath which crustal magma reservoirs are able to develop. Renewed magma recharge after such a stage leads to volcanic unrest, often associated with ground deformation of the caldera floor in the form of 'doming' or uplift of faulted blocks (resurgence). Such phenomena have long been described at numerous caldera-bearing volcanoes, including Long Valley in California, Valles caldera in New Mexico, Phlegraean Fields, Pantelleria and Ischia in Italy, Iwo-jima in Japan, and Tanna in Vanuatu (e.g. Dvorak & Dzurizin, 1997; Molin *et al.*, 2003). Caldera floor resurgence and block uplift can be progressive or discontinuous (e.g. Dvorak & Dzurizin, 1997), can have variable geometry depending of the aspect ratio of the magma intrusions or reservoirs (e.g. Acocella *et al.*, 2000), and can occur without contemporaneous magma extrusion, implying complex relationships between magma replenishment, pressurization of aquifers and hydrothermal systems, as well as local structures and tectonic movements (e.g. Marsh, 1984; Hill *et al.*, 1985). Therefore, improved understanding of these phenomena and their relationships is of fundamental interest for anticipating the eruptive pattern of such caldera-bearing volcanoes and the associated risks.

One suitable site where such processes and relationships can be investigated is Siwi caldera, in Tanna island, where post-caldera eruptive activity (Yasur volcano) and block resurgence have long developed together. Tanna island belongs to the southern segment of the 1200 km long Vanuatu volcanic arc, in the SW Pacific (Fig. 1a). This oceanic island arc has been generated by eastward subduction of the Australian plate beneath the Pacific plate, with associated back-arc extension of the North Fiji basin on the Pacific side (Pelletier *et al.*, 1998; Calmant *et al.*, 2003). The plate convergence rate reaches 11·8 cm a^{-1} at the latitude of Tanna. The island stands 150 km east of the Vanuatu trench and ~130 km above the Benioff zone, and has been built through successive phases of volcanic activity and reef limestone growth. Pliocene–Pleistocene volcanic activity gave rise to the Green Hill and Tukosmeru centers, mainly formed by basalts and andesites (Carney & MacFarlane, 1979; Fig. 1b). A complex pyroclastic series, the Old Tanna ignimbrite (OTI), tracks a major caldera-forming event during this period (Robin *et al.*, 1994). Since the late Pleistocene, volcanic activity has been concentrated in the SE part of Tanna (Fig. 1b). The most important event was a caldera-forming eruption of moderate volume (~1–2 km^3) that produced the Siwi ignimbrite (Carney & MacFarlane, 1979; Nairn *et al.*, 1988; Robin *et al.*, 1994; Allen, 2005). This eruption is still undated but is probably less than 20 kyr old (Nairn *et al.*, 1988). The Siwi pyroclastic sequence, well exposed as a near-continuous 11 km long outcrop along the eastern coast, consists of subaerial pumice-rich pyroclastic flow deposits, separated by a variably welded lithic-rich spatter agglomerate (Allen, 2005). Caldera collapse along the Siwi ring fractures has been followed by a new unrest cycle, with impressive uplift of the central caldera floor, generating the so-called Yenkahe resurgent block (YRB), and by renewed volcanic activity on that horst and along the ring fractures (Carney & MacFarlane, 1979; Nairn *et al.*, 1988; Robin *et al.*, 1994; Fig. 1c).

The Yenkahe resurgent block is an ~6 km long by 3 km wide ENE–WSW elongated horst, with an axial graben that is affected by extensive normal block faulting and widespread hydrothermal manifestations (Fig. 1c). Emerged coral reef terraces present on that structure record its rapid uplift, at a time-averaged rate of 156 mm a^{-1} over the last 1000 years (Chen *et al.*, 1995). Such rapid deformation, involving sharp episodes of co-seismic uplift (e.g. 10–15 m in 1878; Chen *et al.*, 1995), is two orders of magnitude larger than the ground uplift (~1·6 mm a^{-1}) along the NW coast of Tanna island since the late Quaternary (Neef *et al.*, 2003). Therefore, it has a volcanic origin, attributed to replenishment of a magma reservoir, and raises concern about hazards from both further major eruptions and possible landslides (Nairn *et al.*, 1988; Chen *et al.*, 1995). The Yenkahe resurgence ranks amongst the fastest ground deformation observed in caldera-bearing volcanic complexes worldwide: its rate greatly exceeds, for example, the resurgence rates recorded during the 1978–1999 unrest at Long Valley caldera (0·04 m a^{-1}; Hill, 2006), and in the past 33 kyr at Ischia (0·024 m a^{-1}; Gillot *et al.*, 1982). It is comparable with post-caldera uplift at only a few sites such as Iwo-jima volcano in Japan (0·15–0·25 m a^{-1}; Ukawa *et al.*, 2006).

Renewed post-collapse volcanic activity in Siwi caldera has included both effusive and explosive phases, with the formation of pyroclastic cones (Ombus, Yasur). Since about 1400 yr BP, the eruptive activity has been focused at Yasur volcano, located on the western edge of the Yenkahe horst, and rising 360 m above sea level (Fig. 1c). The growth of the Yasur cone itself probably began about 800 years ago, and has continued until now (Nairn *et al.*, 1988). Strombolian or Vulcanian explosive activity has long prevailed at Yasur but has occasionally culminated in more powerful (sub-Plinian) eruptions (Nairn *et al.*, 1988). The 'standard' Yasur activity, first described by Captain Cook in 1774 (Aubert de la Rüe, 1960; Carney & MacFarlane, 1979), consists of recurrent explosions with an average frequency of 1–3 per minute (e.g. Nabyl *et al.*, 1997; Bani & Lardy, 2007), which generate dense ash clouds (Fig. 2a), and expel vesicular scoriae and decimeter- to

Downloaded from http://petrology.oxfordjournals.org/ by guest on March 22, 2015

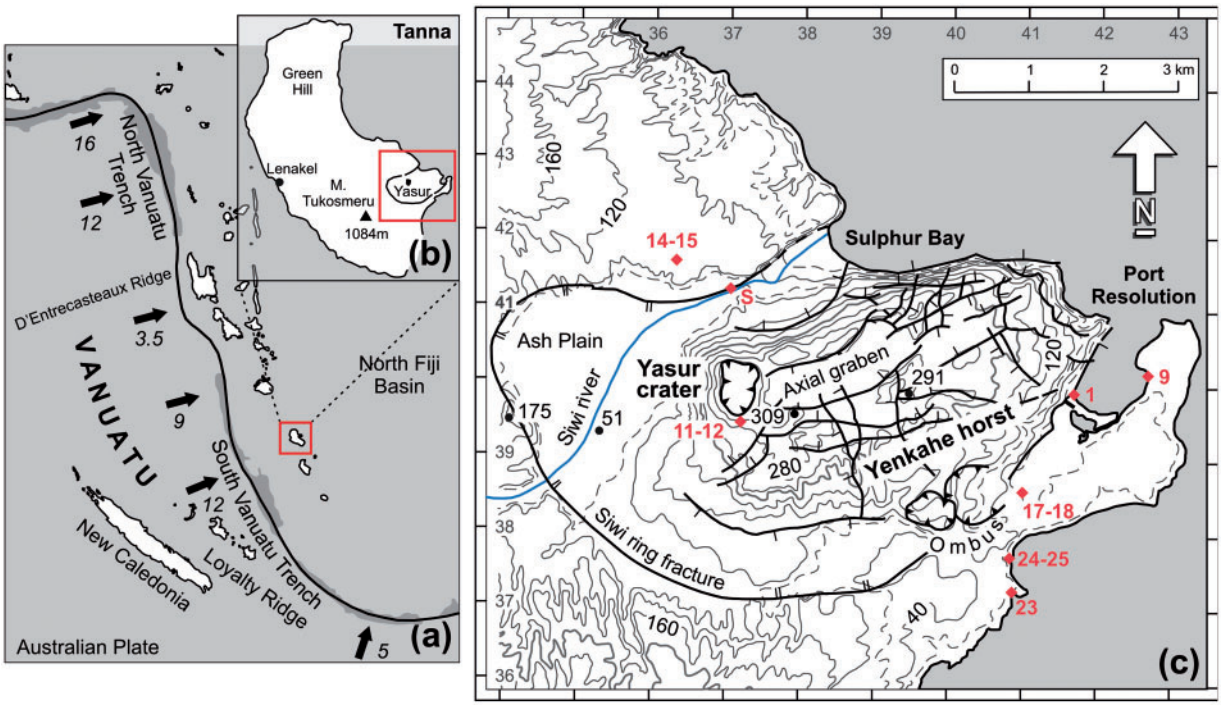

Fig. 1. (a) Map showing the Vanuatu (previously New Hebrides) arc in the SW Pacific, the position of the 6000–7000 m deep Vanuatu Trench, convergence rates (indicated by arrows in cm a^{-1}), and the location of Tanna volcanic island, which is built up on a 1000 m deep plateau; redrawn from Pelletier *et al.* (1998) and Calmant *et al.* (2003). (b) Schematic map of Tanna island with the locations of the main volcanic centers, redrawn from Carney & MacFarlane (1979). (c) Map of southeastern Tanna showing the Yasur cone and Yenkahe resurgent block, bounded by the Siwi caldera ring fracture; redrawn from Nairn *et al.* (1988) and Allen (2005). Diamonds indicate the sample sites of the Siwi ignimbrite sequence, and Yasur products of the early (>1400 to 800 yr BP sequence; S) and present-day activities.

meter-sized bombs that occasionally reach the volcano flanks (Fig. 2b). Lava flow effusions are rare (Carney & MacFarlane, 1979).

Until now, there have been few studies of the Yasur activity and its broader relationship with the evolution of the Siwi caldera system. Here, we report new data from a systematic study of solid products and magmatic volatiles from both the early and current Yasur eruptive activity, and the Siwi ignimbrite sequence. Our objectives were to (1) determine the magma feeding composition and differentiation processes, (2) assess the abundances of dissolved and exsolved volatiles, (3) quantify the magma volumes sustaining the current Yasur activity and gas emissions, and (4) elucidate the possible relationships between magma supply and storage and the Yenkahe block resurgence. Rock sampling and gas measurements were performed during a field campaign in October 2007 and different approaches were combined to investigate the magma petrology and geochemistry, dissolved volatiles in melt inclusions and glassy matrices, and the present-day crater gas emissions. Altogether, our results allow us to propose a quantitative model for the magma feeding system of the Siwi–Yasur caldera complex, and to discuss its relationship with continuing Yenkahe block resurgence.

SAMPLES AND MEASUREMENTS

Solid volcanic products

Sample location and description

The early (>1400 to 800 yr BP) Yasur volcanic products were sampled from a >10 m thick sequence on the northern bank of Siwi river, about 1 km NNW from Yasur crater (19·5161°S, 169·4470°E; Fig. 1c). This sequence was exposed to the open air after catastrophic drainage of the former Siwi water lake in 2000, which deeply eroded the Siwi riverbed. It includes two unconformities ascribed to pauses in volcanic activity. An analogous sequence had previously been identified by Nairn *et al.* (1988) and correlated with a more distal section (4 km NNW from Yasur cone) where the pauses have been dated at 1409 ± 80, and 804 ± 56 years BP, respectively (^{14}C conventional ages). Correlation between our samples and the stratigraphic logs provided by Nairn *et al.* (1988) is shown in Fig. A in the Electronic Appendix (available for downloading at http://www.petrology.oxfordjournals.org). Deposits older than 1400 years consist of ash beds containing fibrous lapilli lenses (TAN 3), and scattered centimetre-sized scoriae (TAN 8). Deposits between 1400 and 800 years BP are mainly formed of alternating centimetres-thick fall layers made of either fine to coarse ash or fibrous to equant scoria lapilli

Downloaded from http://petrology.oxfordjournals.org/ by guest on March 22, 2015

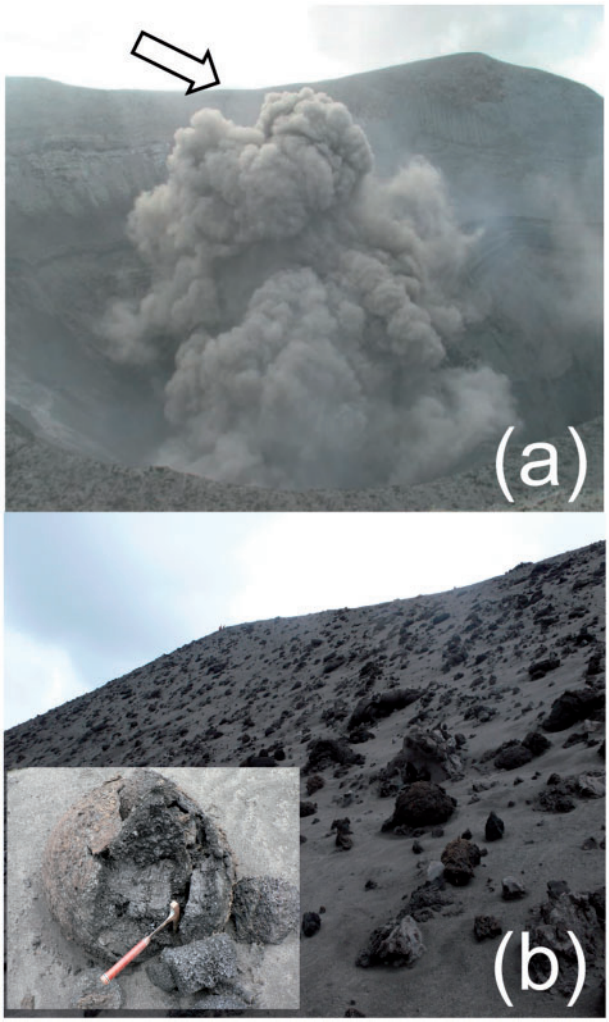

Fig. 2. (a) Ash-laden cloud at Yasur crater (21 October 2007). Gas measurements were carried out during typical Yasur Strombolian activity (1 explosion per minute), on the crater outer rim as indicated by the arrow. (b) Bombs on Yasur flank; hammer for illustration of the scale.

(TAN 4 and 5). The presence of accretionary lapilli and vesiculated tuffs points to repeated involvement of external fluids (groundwater or the hydrothermal system) in driving the explosive activity. The uppermost 60 cm thick layer, made up of equant scoria lapilli (TAN 6), is believed to be equivalent to the sub-Plinian deposit described by Nairn *et al.* (1988). On the southern side of the Siwi river, we sampled two additional scoria fall layers (TAN 20 and 21) that directly overlie a plagioclase-phyric lava flow forming the riverbed (TAN 19; 19·5168°S, 169·4457°E). These deposits should be related to the early Yasur activity.

As representative samples for the past 800 years of persistent eruptive activity at Yasur cone itself, we collected and analyzed both fibrous lapilli (TAN 14 and 15) deposited on the surface ~1·5 km NW from the vent, along the main ash dispersal axis, and proximal explosive products. The latter include a bomb (TAN 10, Fig. 2b), and centimetre-sized highly vesicular scoriae (TAN 12) that fell on the crater rim.

We also collected and analyzed pumices from the ignimbrite deposits related to Siwi caldera collapse (hereafter referred to as the Siwi sequence). Pumices from the upper pyroclastic flow deposit (TAN 23; 19·5534°S, 169·4830°E), intermediate spatter-rich agglomerate (TAN 24), and lower pyroclastic deposits (TAN 25; 19·5493°S, 169·4826°E) were sampled along the SE coast (Fig. 1c). This succession is equivalent to that described by Allen (2005). Additional pumice samples were taken from meter-scale pyroclastic flow deposits cropping along the eastern side of Port Resolution bay (TAN 9; 19·5267°S, 169·5040°E), and on the Siwi ring fracture (TAN 17 and 18; 19·4126°S, 169·4842°E). These two latter superimposed pyroclastic flows are attributed to late stages of the Siwi ignimbrite eruption on the basis of the texture of their junvenile components. Finally, we sampled another ~7 m thick pyroclastic sequence along the Yenkahe horst southern border at Port Resolution bay (TAN 1; 19·5292°S, 169·4908°E), formed by coarse-grained pumice-rich lenses interbedded with ash layers. This sequence, which has not been previously described, overlies laminated black sands with shell fragments. It was most probably emplaced in shallow seawater inside the Siwi caldera and is considered here as related to post-caldera activity, from volcanic vents located on the Yenkahe horst, and preceding the building of the Yasur cone.

Analytical procedures

Major and trace element analyses of Siwi and Yasur bulk-rocks were carried out at the Centre de Recherches Pétrographiques et Géochimiques (SARM) in Nancy (France), by inductively coupled plasma optical emission spectroscopy (ICP-OES) and inductively coupled plasma mass spectrometry (ICP-MS), respectively (Carignan *et al.*, 2001). A second set of trace element data was acquired on pairs of Yasur bulk scoria and mechanically separated matrices using ICP-MS at Laboratoire Pierre Süe (Saclay, France). Matrix fragments were handpicked under the binocular, then aliquots of 50 mg of glass and powdered host bulk-rocks were analyzed during the same run. The former trace element dataset is reported in Table 1, and the second one as Electronic Appendix 1.

Major elements of minerals, melt inclusions, and matrix glasses were analyzed using a SX50 CAMECA electron probe (Camparis, Jussieu, France). In glasses and minerals, they were measured with a 10 nA defocused beam and a 30 nA focused beam, respectively, and a counting time varying from 10 to 25 s. The concentrations of S, Cl and P were determined with a 30 nA defocused beam and a longer counting time (120–200 s) on peak, and their accuracy was checked by analyzing reference glasses (basalts

Downloaded from http://petrology.oxfordjournals.org/ by guest on March 22, 2015

Table 1: Major and trace element compositions of bulk-rocks

	Yasur							Siwi ignimbrite sequence							Lava	2·4 Ma	0·67 Ma	0·23 Ma
	Distal products*					Prox. products*		Pumices										
Sample:	TAN 3	TAN 6†	13/1-B†	TAN 21	TAN 8	TAN 12	TAN 10	TAN 1	TAN 17	TAN 18	TAN 9	TAN 23	TAN 24	TAN 25	TAN 19	TAN 75‡	TAN 93	TAN 82
	Bas-Tα	Bas-Tα	Bas-Tα	Bas-Tα	Tα	Bas-Tα	Bas-Tα	Bas-Tα	Bas-Tα	Bas-Tα	Tα	Tα	Tα	Tα	Tα	Bas	Bas	Bas-Tα
SiO_2 (wt %)	55·53	55·65	55·59	56·84	58·59	55·85	54·53	55·26	56·39	56·39	58·79	59·87	60·22	58·05	56·20	49·07	47·51	52·01
Al_2O_3	15·85	15·83	16·20	16·14	15·10	18·77	19·46	16·37	16·30	16·16	15·35	15·32	15·39	15·47	16·25	19·61	16·08	18·78
Fe_2O_3	9·45	9·48	9·49	8·89	8·67	7·70	7·20	9·00	8·92	8·90	8·83	8·49	8·61	8·91	8·94	11·48	12·56	10
MnO	0·16	0·17	0·17	0·16	0·16	0·14	0·12	0·16	0·16	0·16	0·18	0·19	0·19	0·19	0·16	0·21	0·22	0·17
MgO	2·63	4·10	4·03	3·00	2·68	2·36	2·13	2·95	2·86	2·83	2·14	2·03	2·03	2·07	2·89	4·57	7·77	3·67
CaO	5·43	7·37	7·09	6·54	5·50	7·47	7·93	6·52	6·36	6·25	4·91	4·67	4·70	4·73	6·41	10·39	12·46	9·9
Na_2O	3·67	3·62	3·57	3·84	3·95	3·85	3·87	3·81	3·87	3·87	4·08	4·28	4·29	4·16	3·83	2·76	1·83	3·3
K_2O	3·13	2·64	2·61	2·93	3·38	2·53	2·39	2·96	2·94	2·96	3·61	3·83	3·85	3·77	2·94	0·92	0·59	1·26
TiO_2	0·95	0·85	0·82	0·87	0·94	0·70	0·65	0·87	0·84	0·85	0·88	0·93	0·93	0·91	0·84	0·82	0·82	0·71
P_2O_5	0·53	0·43	0·41	0·47	0·54	0·42	0·38	0·48	0·50	0·50	0·62	0·65	0·66	0·65	0·48	0·19	0·16	0·22
LOI	1·7	0·3	n.d.	0·9	0·5	−0·2	0·0	0·8	0·0	0·1	−0·2	0·0	0·1	−0·2	−0·1	0·08	0·80	0·04
Total	99·06	100·44	99·98	100·54	100·03	99·63	98·60	99·15	99·14	98·92	99·22	100·25	100·95	98·73	98·86	99·19	100·80	99·22
$Na_2O + K_2O$	6·8	6·3	6·2	6·8	7·3	6·4	6·3	6·8	6·8	6·8	7·7	8·1	8·1	7·9	6·8	3·7	2·4	4·6
Ba (ppm)	600	464		621	560	570	484	544	659	649	700	771	781	699	644	237	120	320
Ce	34·2	26·1		35·7	32·2	31·0	24·3	30·9	38·2	37·9	40·3	46·0	46·4	40·7	37·6	17·7	8·1	15·3
Cs	1·4	1·1		1·5	1·5	1·3	1·1	1·3	1·6	1·6	1·8	2·1	2·1	1·8	1·4	0·34	0·31	0·39
Co	17	21		20	15	18	15	18	20	19	16	17	16	15	19	34	45	28
Cr	b.d.l.	49		14	9	26	20	10	20	23	6	12	12	b.d.l.	11	8	81	5
Rb	42	34		46	44	40	33	40	49	49	53	61	60	53	48	10	7·7	14
Sr	469	522		643	431	750	720	537	653	633	452	485	489	436	640	1039	424	760
Dy	4·4	3·5		4·5	4·0	3·7	3·2	3·9	4·7	4·6	5·1	5·6	5·8	5·3	4·6	3·0	2·0	3·0
Er	2·7	2·0		2·7	2·4	2·2	1·9	2·3	2·7	2·7	3·1	3·4	3·4	3·1	2·7	1·8	1·1	1·9
Eu	1·4	1·2		1·6	1·3	1·4	1·2	1·4	1·6	1·6	1·6	1·8	1·9	1·6	1·6	1·1	0·7	1·0
Gd	4·9	3·8		4·9	4·4	4·1	3·5	4·4	5·1	5·1	5·4	6·2	6·2	5·7	5·1	3·5	1·7	0·6
Hf	3·5	2·4		3·2	3·1	2·7	2·3	2·9	3·4	3·3	3·9	4·1	4·2	4·0	3·4	1·6	0·8	1·5
Ho	0·9	0·7		0·9	0·8	0·8	0·6	0·8	0·9	0·9	1·1	1·1	1·2	1·1	0·9	0·7	0·5	0·58
La	15·3	11·7		16·0	14·4	13·9	11·0	14·0	17·2	17·1	17·7	20·4	20·7	18·2	16·9	6·56	3·54	7·36
Lu	0·44	0·33		0·43	0·39	0·36	0·3	0·4	0·45	0·44	0·5	0·53	0·55	0·50	0·44	0·26	0·20	0·28

(continued)

Downloaded from http://petrology.oxfordjournals.org/ by guest on March 22, 2015

Table 1: Continued

	Yasur							Siwi ignimbrite sequence							Lava	2·4 Ma	0·67 Ma	0·23 Ma
	Distal products*					Prox. products*		Pumices										
Sample:	TAN 3	TAN 6†	13/1-B†	TAN 21	TAN 8	TAN 12	TAN 10	TAN 1	TAN 17	TAN 18	TAN 9	TAN 23	TAN 24	TAN 25	TAN 19	TAN 75‡	TAN 93	TAN 82
	Bas-Tα	Bas-Tα	Bas-Tα	Bas-Tα	Tα	Bas-Tα	Bas-Tα	Bas-Tα	Bas-Tα	Bas-Tα	Tα	Tα	Tα	Tα	Tα	Bas	Bas	Bas-Tα
Nb	1·4	1·1		1·4	1·4	1·3	1·0	1·2	1·6	1·5	1·7	1·9	1·9	1·7	1·5	0·64	0·36	0·68
Nd	21·6	17·0		22·7	20·5	19·4	15·7	19·8	24·2	24·2	25·6	29·2	29·1	25·4	24·0	13·1	6·47	10·6
Pb	15·4	11·1		15·0	14·6	14·0	10·9	13·0	14·9	15·0	16·8	18·6	19·0	17·9	14·8	4·8	2·6	5·6
Pr	4·9	3·4		5·1	4·2	4·3	3·5	4·4	5·4	5·4	5·7	6·4	6·6	5·7	5·3	2·5	1·2	2·2
Sm	5·2	4·1		5·5	4·8	4·7	3·7	4·7	5·8	5·8	6·1	6·9	7·0	6·1	5·8	3·2	1·7	3·0
Ta	0·11	0·08		0·10	0·10	0·09	0·08	0·10	0·12	0·11	0·13	0·14	0·14	0·13	0·11	0·04	0·03	0·05
Tb	0·73	0·58		0·75	0·66	0·64	0·53	0·65	0·78	0·79	0·85	0·95	0·96	0·85	0·77	0·46	0·27	0·56
Th	2·55	1·80		2·54	2·30	2·12	1·72	2·17	2·62	2·66	2·92	3·27	3·29	2·96	2·57	0·89	0·41	0·97
Tm	0·40	0·31		0·39	0·36	0·33	0·3	0·4	0·41	0·41	0·5	0·51	0·51	0·5	0·41	0·25	0·27	0·28
U	1·44	1·02		1·37	1·32	1·14	0·98	1·25	1·45	1·45	1·67	1·78	1·81	1·68	1·42	0·30	0·22	0·49
Y	25·9	20·8		26·6	24·0	22·7	18·5	23·2	28·0	27·4	30·3	34·1	34·3	30·7	27·4	17·8	12·9	18·2
Yb	2·8	2·1		2·7	2·5	2·3	2·0	2·4	2·8	2·8	3·3	3·4	3·5	3·2	2·8	1·7	1·1	1·8
Zr	116	90		116	114	102	81	101	126	123	137	156	157	136	123	49	25	51
La/Sm	2·9	2·8		2·9	3·0	3·0	3·0	3·0	3·0	2·9	2·9	3·0	3·0	3·0	2·9	2·1	2·1	2·5
Ba/Th	235	258		244	243	269	281	251	252	244	239	236	237	236	250	266	293	330
Th/Ta	23	23		25	22	24	20	23	23	24	23	23	24	23	24	21	14	21
Th/Nb	1·8	1·6		1·8	1·7	1·7	1·7	1·8	1·7	1·7	1·8	1·7	1·7	1·7	1·7	1·4	1·1	1·4
La/Nb	10·7	10·4		11·4	10·6	11·0	10·8	11·7	11·1	11·1	10·6	10·7	10·9	10·7	11·3	10·3	9·8	10·8
Ba/La	39·2	39·8		38·7	38·7	41·0	44·0	38·8	38·3	38·1	39·6	37·7	37·7	38·4	38·1	36·1	33·9	43·5
Nb/Yb	0·52	0·54		0·52	0·54	0·55	0·52	0·49	0·55	0·55	0·51	0·56	0·55	0·52	0·54	0·39	0·32	0·38

Analytical uncertainties (1σ) are <10% for Th, Ta, Hf, Cs, Co and Cr; <8% for U and Ba; <5% for the others. Bas, basalt; Bas-Tα, basaltic-trachyandesite; Tα, trachyandesite. LOI, loss on ignition; b.d.l. below detection limit; n.d., not determined.
*Yasur distal and prox. products refer, respectively, to distal scoria deposits and proximal bombs and scoriae on the volcano flanks and crater rims.
†Lapilli sample (13/1-B) from the sub-Plinian fall deposit described by Nairn et *al.* (1988), equivalent to our sample TAN 6.
‡TAN 75, 93, 82, bulk analyses from Peate *et al.* (1997).

Downloaded from http://petrology.oxfordjournals.org/ by guest on March 22, 2015

AlV981R23 and Vg2, pantellerite KE12). Fluorine was determined by coupling two TAP crystals, in a scanning mode, with 10 kV voltage, 60 nA beam current, 15 μm beam size, and 500 s counting time. Analyses were calibrated against reference glasses containing from 950 to 4250 ppm F (Spilliaert *et al.*, 2006). The relative errors are ≤10% for S and Cl, and 10% for F. The detection limits are 80 ppm for S and Cl, and 170 ppm for F.

Some glassy matrices and minerals were also analyzed and mapped with a Philips XL30 scanning electron microscope equipped with an EDAX DX 4 system (Dpt Scienze della Terra, Pisa, Italy).

Dissolved H_2O contents were determined with micro-Raman spectroscopy, using a Renishaw inVia instrument (Saclay, France). The spectrometer is fitted to a Leica microscope with a 100× objective to excite and collect the signal from a very small area (about 1 μm in diameter). Analyses were performed at the sample surface in confocal mode. The excitation source was a green diode laser (532 nm) filtered to deliver a low power (*c.* 7 mW) on the sample during short counting times (<100 s). Selected analytical conditions minimize scatter from the embedding medium and prevent sample heating and oxidation. The intensity of the H_2O_T band (3580 cm^{-1}) and its scaling with respect to the band for the silicate network (980 cm^{-1}) were determined with external analytical procedures (Mercier *et al.*, 2009). Calibration was made against a set of basaltic and andesitic glass standards (Mercier *et al.*, 2010). One to three analyses were performed, prior to any other measurements to avoid H_2O loss, for each melt inclusion and then averaged. Errors propagated on the external calibration procedures range between 6 and 10%.

Finally, dissolved carbon concentrations were determined with the Saclay nuclear microprobe (France), using the $^{12}C(d, p)^{13}C$ nuclear reaction (Métrich & Wallace, 2008). Analyses were made in scanning mode, with a 5 μm beam. Areas in melt inclusions previously analyzed for S, Cl, F with a high electron beam current were avoided. The integrated charge varied from 2 to 1·5 μC, implying a corresponding minimum detection limit of 60–70 ppm of CO_2. Carbon concentrations were calibrated against a scapolite standard (6800 ppm C) and a water-bearing Etna basaltic glass (EtII-1) containing 300 ± 30 ppm C (Spilliaert *et al.*, 2006). The latter glass concentration is reproduced with 10% precision.

The temperatures of melt entrapment were determined from optical thermometry measurements on melt inclusions hosted in olivine and plagioclase in the Yasur products. Experiments were carried out under a Leitz heating stage purged with Ar–1% H_2 gas flow. Temperatures were measured with a $Pt–Pt_{90}Rh_{10}$ thermocouple (±10°C), and calibrated against the melting points of Ag (961·8°C) and Au (1063·8°C). It is known that the homogenization temperature (T_{hom}) of olivine-hosted melt inclusions—when the shrinkage bubble vanishes—increases with time because of olivine crystal deformation (Massare *et al.*, 2002). Actually, the temperature (T_{hom}) measured on melt inclusions hosted in TAN 6 olivines is 10–50°C higher when several (1–9) heating–cooling cycles have been completed on a single crystal. A heating rate of 18·5°C min^{-1} was thus chosen to minimize this effect. Experiments were also carried out with a slower heating rate (6°C min^{-1}) from 1050°C to T_{hom} to verify that no kinetic effects may have affected our measurements. A total of 30 heating experiments were conducted on double-faced polished crystals whose inclusions were preserved enclosed.

Yasur crater gas emissions

Chemical composition of emitted gases

The chemical composition of Yasur gas emissions was determined from *in situ* analysis and sampling of the volcanic plume at the crater rim, ~150 m downwind of vent A (Fig. 2a). This vent was the most vigorously active (one explosion every minute, on average) and the main source of degassing during our two series of measurements, on 21 and 29–30 October 2007.

The plume concentrations in water vapor, CO_2 and SO_2 were measured continuously with MultiGas instruments (Shinohara, 2005; Aiuppa *et al.*, 2007, 2008; Shinohara *et al.*, 2011), which combine different gas sensors in a home-made box (INGV-type used on 21 October and GSJ-type used on 29–30 October). Volcanic gases were pumped at an average flow rate of 0·6 l min^{-1} and analyzed with these systems. An LI-840 closed-path NDIR spectrometer measured both CO_2 (range 0–3000 ppmv; accuracy ± 1·5%), and H_2O (range 0–80 ppt; accuracy ± 1·5%). SO_2 was measured with different electrochemical sensors (3ST/F-Cod.TD2D-1A and KTS-5l2P, respectively) that have similar performances in concentration range, noise level and response (Shinohara *et al.*, 2011). The signals from all sensors were recorded and stored every 2 s (INGV-type) and 1 s (GSJ-type) on a data-logger.

MultiGas sensing on 21 October 2007 provided ~4500 measurements of each gas species during 135 min of volcanic activity. The data for CO_2 and H_2O were post-processed by subtracting the concentrations in ambient air from the bulk recorded signals. Air background concentrations were constrained by fitting a polynomial function to the subset of CO_2 and H_2O data for which SO_2 concentration is zero (given that SO_2—a typical component of magmatic gas emissions—is absent in standard atmosphere). The resulting air concentrations were fairly constant for CO_2 (384–387 ppm) but more variable for H_2O (19–440–21–020 ppm). Similar data handling was applied to the 29–30 October datasets; however, these were affected by higher and more randomly changing background H_2O.

Downloaded from http://petrology.oxfordjournals.org/ by guest on March 22, 2015

During this second survey, H_2 and H_2S could additionally be determined with the sensor configuration described by Shinohara *et al.* (2011).

Filter pack sampling of the volcanic gas was carried out in tandem with MultiGas sensing to measure time-averaged SO_2, HCl and HF concentrations. Sampling was performed for 45–60 min, by pumping the volcanic plume at an average flow rate of 5 l min^{-1} through alkali-impregnated filters (e.g. Aiuppa *et al.*, 2005). Six filter series were collected on 21 October and seven on 29–30 October. In the laboratory, the filters were leached with bi-distilled water and H_2O_2, to elute S, Cl and F. The leachates were then analyzed by ion chromatography for SO_4^{2-} and Cl^- and by ion selective electrode for F^- (Aiuppa *et al.*, 2005).

SO_2 emission rate

The SO_2 emission rate from Yasur was determined by differential absorption UV spectroscopy (DOAS), during repeated traverses under the volcanic plume with a four-wheel-drive vehicle. The UV spectrometer (Ocean Optics USB2000, Serial No. 2196) spanned a 280–400 nm spectral range, with a resolution of 0·5 nm (full width at half-maximum). It was coupled by a fiber optic bundle to a telescope fixed outside the vehicle and pointed to zenith. Exposure time for single spectra was 200 ms, and we co-added eight spectra to enhance the signal-to-noise ratio. The position of each UV spectrum was obtained from the log of a continuously recording global positioning system (GPS) unit. SO_2 column amounts were retrieved following standard DOAS spectral procedures (e.g. Galle *et al.*, 2003; Bani & Lardy, 2007). The best-fitting window for SO_2 retrieval (307·7–335·1 nm) was constrained from near random fit residual structure with minimal standard deviation. The SO_2 reference spectrum was obtained by convolving a high-resolution SO_2 spectrum with our instrument line shape, and then removing the low-frequency component using the Ocean Optics WinDOAS software. The observed SO_2 column amounts were then projected onto the plane perpendicular to the plume transport direction, and the SO_2 emission rate for each traverse was obtained by scaling the integrated column amounts across this plane with the plume speed. Plume speeds were directly obtained from simultaneous wind speed measurements on top of Yasur volcano, using a hand-held anemometer ($\pm$0·1 m s^{-1}). The overall error on each SO_2 flux series (given in Electronic Appendix 2) includes errors on the wind speed and DOAS spectral analysis (Galle *et al.*, 2003).

MINERALOGY AND MAGMA GEOCHEMISTRY

Bulk-rocks and matrices

Juvenile products from the early ($\leq$1400 years) and present-day Yasur activity show a limited compositional range, with SiO_2 between 54·5 and 56·8 wt % (Table 1). In the Total Alkali–Silica (TAS) diagram, they plot in the field of basaltic-trachyandesite, except one sample (TAN 8), which has a pure trachyandesitic composition (58·6 wt % SiO_2; Table 1). Yasur bulk-rocks also display restricted variations in trace elements (Figs 3 and 4), even though distal and proximal explosive products differ in texture and crystal content.

The Yasur distal products contain a few per cent of plagioclase, clinopyroxene and olivine phenocrysts, embedded in highly vesicular glassy matrices with trachyandesitic composition (SiO_2 from 56·5 to 58·5 wt %; Table 2). Systematic analyses (88) of plagioclase crystals in the TAN 6 sample show that most of them are normally zoned, from An_{66} to An_{57}. Rare crystals were found to have a more calcic core (An_{80} to An_{87}). Clinopyroxene ($Wo_{41·1–40}$ $Fs_{12·3–15·3}$) and olivine ($Fo_{75·2–72·7}$ in the cores to $Fo_{75–72·6}$ in the rims) display limited compositional variations. Olivine also occurs as inclusions in clinopyroxene and plagioclase $An_{68–60}$, together with Fe–Ti oxides (Usp 16%). We attempted to precisely quantify the crystal content of these scoria lapilli by analyzing the trace element content of five pairs of the bulk clasts and their mechanically separated matrices (TAN 4, 5, 14, 15 and 20), representative of the past 1400 years of eruptive activity (Electronic Appendix 1). These selected samples are all similar in their incompatible element concentrations (i.e. U, Th, Nb, La, Ce), normalized trace element patterns (Fig. 4), large ion lithophile element (LILE) enrichment, and negative Nb anomaly (Nb/Nb* = 0·26 in bulk clasts and 0·31 in matrices, where Nb* refers to the normal mid-ocean ridge basalt (N-MORB) value of 3·507 ppm; Hofmann, 1988). This homogeneity indicates a nearly constant extent of crystallization over time. Using the equation for equilibrium crystallization $[C_i = C_{i0}/(Di + F(1 - D_i)]$, with C_{i0} and C_i being the average thorium concentrations in the bulk clasts (2·1 ppm) and matrices (2·5 ppm), Di the Th bulk partition coefficient ($D^{\text{mineral/melt}} \sim 0·1$) and F the proportion of residual melt, we find that the Yasur distal scoriae contain 10% of crystals at most. This proportion agrees with the difference in K_2O content between the bulk samples and their matrices (e.g. TAN 6 and 21; Tables 1 and 2), indicating that K_2O is also a reliable tracer of magma differentiation.

Yasur proximal products prevalently contain plagioclase ($An_{62·4–55}$) phenocrysts, reaching 5 mm in size, which coexist with rare olivine (Fo_{67}), clinopyroxene ($Wo_{38·8–39·6}$, $Fs_{17·8–16·6}$) and Fe–Ti oxide (Usp 26–27%). Consequently, their matrices, when preserved glassy in vesicular scoria clasts (as verified by SEM imaging), are depleted in Al_2O_3 (14·8 wt %; Table 2). From the average K_2O contents of the matrix glasses (3·7 wt %) and bulk-rocks (2·5 wt %), we infer an average crystal content of $\sim$32% in these samples.

Downloaded from http://petrology.oxfordjournals.org/ by guest on March 22, 2015

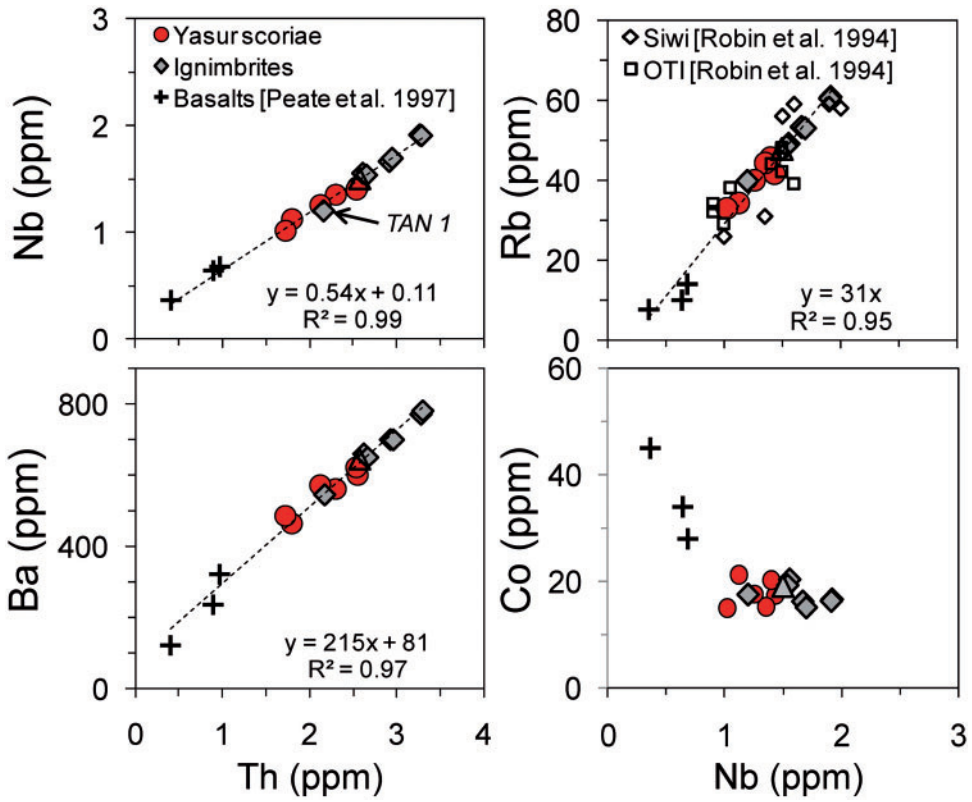

Fig. 3. Selected trace element variations in Yasur products, Siwi ignimbrite samples, and a post-caldera lava flow. Basalts from the oldest volcanic edifices (Peate *et al.*, 1997) dated at 2·4, 0·67 and 0·23 Ma, and pumices of the undated Old Tanna ignimbrite (OTI; Robin *et al.*, 1994) plot on the same trend of magma differentiation.

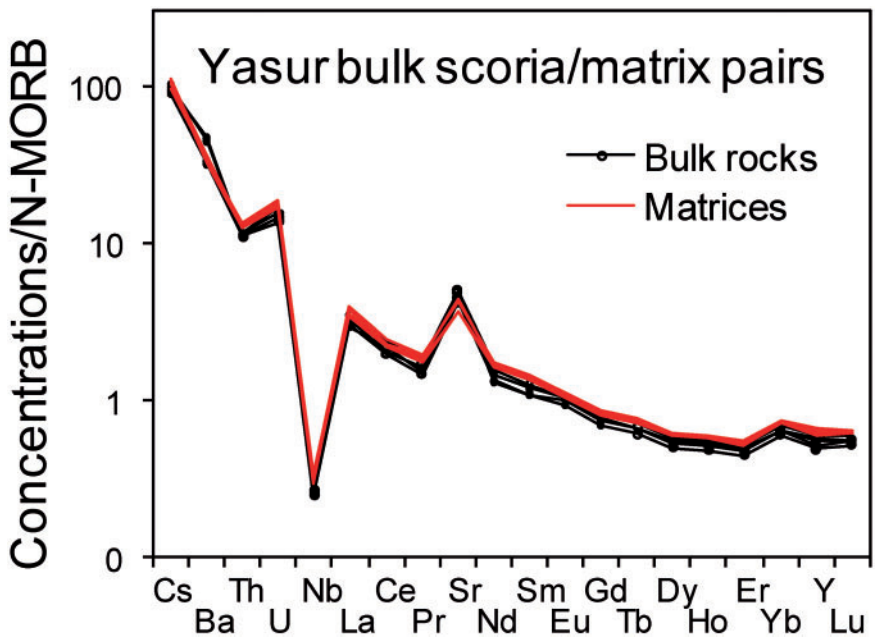

Fig. 4. Trace element patterns of bulk scoriae (TAN 4, 5, 14, 15, 20), and of their mechanically separated matrices for the early and present-day activity of Yasur. The element concentrations are normalized against the N-MORB values (Hofmann, 1988).

Downloaded from http://petrology.oxfordjournals.org/ by guest on March 22, 2015

Table 2: Representative compositions of glassy matrices of Yasur and Siwi sequence products

Sample	*N*	SiO_2	TiO_2	Al_2O_3	FeO_{tot}	MnO	MgO	CaO	Na_2O	K_2O	P_2O_5	S	Cl	F	H_2O	Total	S/Cl	Cl/F
*Yasur D-products**																		
TAN 6 av.†	15	56·54	0·88	15·64	8·50	0·16	3·15	6·15	3·88	2·85	0·52	0·016	0·083	n.d.	n.d.	98·39	0·2	
		(42)	(4)	(13)	(27)	(4)	(18)	(7)	(21)	(17)	(1)	(1)	(6)					
TAN 4 T6/3-1‡	4	57·98	1·02	15·60	8·38	0·16	2·79	5·64	3·87	2·69	0·58	0·023	0·086	0·034	0·2	99·04	0·3	2·5
TAN 4 T6/3-2	6	58·49	0·97	15·49	8·33	0·20	2·79	5·52	3·87	2·60	0·57	0·022	0·093	0·043	0·3	99·33	0·2	2·1
TAN 4 T3/3-1	6	57·37	0·97	15·44	8·22	0·19	2·64	5·68	3·87	2·92	0·58	0·013	0·089	0·031	0·3	98·29	0·1	2·9
TAN 21 av.	19	57·74	1·01	15·15	8·15	0·18	2·70	5·55	4·11	3·32	0·61	0·018	0·080	n.d.	n.d.	98·61	0·2	
		(13)	(5)	(16)	(14)	(2)	(2)	(7)	(4)	(3)	(1)	(2)	(1)					
*Yasur P-products**																		
TAN 12 av.	14	59·19	0·95	14·79	8·58	0·16	2·13	5·33	3·68	3·70	0·68	0·006	0·046	0·036	0·16	99·43	0·1	1·3
		(39)	(9)	(17)	(21)	(4)	(28)	(17)	(3)	(6)	(1)	b.d.l.	(2)	(10)	(1)			
Siwi igimbrite sequence																		
TAN 1 vesiculated clasts	20	58·27	0·91	15·49	7·74	0·19	2·33	4·96	4·12	3·57	0·61	0·033	0·110	n.d.	n.d.	98·33	0·3	
		(22)	(1)	(10)	(11)	(4)	(4)	(14)	(6)	(4)	(1)	(4)	(5)					
TAN 17 vesiculated clasts	4	57·30	0·93	15·43	8·03	0·16	2·32	5·16	4·29	3·57	0·60	0·033	0·107	n.d.	n.d.	97·92	0·3	
TAN 23 obsidian clasts	8	60·28	0·85	15·60	7·16	0·13	1·79	4·13	4·33	3·73	0·66	0·031	0·064	n.d.	0·4	99·13		
TAN 23 vesiculated clasts	10	60·18	0·85	15·53	7·22	0·18	1·73	4·14	4·26	3·95	0·66	0·026	0·062	n.d.	n.d.	98·78		
TAN 23 dense clasts	10	60·52	0·87	15·40	7·00	0·18	1·68	4·00	4·33	3·90	0·65	0·026	0·060	n.d.	n.d.	98·63		
Allen (2005)		61·0	0·9	15·9	6·6	0·18	1·8	4·2	3·6	4·1	0·6					98·85		
TAN 23, glasses surrounding crystals																		
TAN 23-1 (Fo_{59})§	4	60·94	0·81	15·00	7·30	0·15	1·60	3·89	4·30	4·09	0·71	0·027	0·070	n.d.	1·1	99·95	0·4	
TAN 23-12 (Fo_{57})	4	61·77	0·84	14·78	7·56	0·30	1·49	3·57	4·09	4·17	0·65	0·030	0·078	n.d.	1·2	100·55	0·4	
TAN 23-2 (Fo_{70})	4	58·37	0·92	15·33	7·60	0·20	2·27	5·12	4·19	3·57	0·61	0·038	0·104	n.d.	1·0	99·30	0·4	
TAN 23-11 (Fo_{72})	4	57·01	0·91	15·21	8·07	0·27	2·53	4·92	4·43	3·45	0·62	0·028	0·111	n.d.	n.d.	97·54	0·3	

*D and P-products refer to distal and proximal scoriae, respectively.
†Averaged analysis performed in several fragments, with standard deviation values in parentheses (i.e. 42 for 56·54 ± 0·42).
‡Traverses between bubbles in different vesiculated pumice clasts.
§The composition of the olivine is indicated in parentheses.
N, number of analysis per fragment; b.d.l., below detection limit; n.d., not determined.

Pumices from the Siwi ignimbrite sequence display a wider range in major and trace element compositions (Table 1). The least evolved samples (TAN 17, 18, 1), with basaltic trachyandesitic compositions ($SiO_2 \leq 56$ wt %, $K_2O = 2{\cdot}95$ wt %), closely resemble Yasur products in terms of both major and trace elements (Fig. 3). Their matrices are slightly more evolved (3·4 wt % of K_2O, Table 2). Although a complete database for the mineral chemistry of these pumices is not available, the olivine crystals ($Fo_{74–69}$) analyzed in samples TAN 17 and TAN 1 are either similar to or slightly more Fe-rich than olivines in the Yasur distal products.

The most evolved Siwi samples ($SiO_2 = 60$ wt %, $K_2O = 3{\cdot}6–3{\cdot}8$ wt %), with the highest concentrations in incompatible elements (Fig. 3), are trachyandesitic pumices (TAN 23, 24, 25, and 9). Their matrix glasses and obsidian shards, extensively analyzed in the crystal-poor sample TAN 23, have a very homogeneous composition (Table 2) equivalent to that of the host bulk pumice, as previously reported by Robin *et al.* (1994) and Allen (2005). The equilibrium paragenesis is made of Na-rich plagioclase (An_{54}) associated with Fe-rich olivine (Fo_{57}) and clinopyroxene ($Wo_{39·8}$, $Fs_{21·5}$). Each of these minerals includes Fe–Ti oxide (usp < 30%), Cu-rich sulfide and fluorapatite micro-crystals that occasionally themselves contain melt inclusions. However, we also discovered in these samples some homogeneous or slightly normally zoned olivine crystals that are noticeably richer in Mg (from $Fo_{70–72}$ to $Fo_{77–80}$). The glassy envelope coating these crystals, when preserved, is also less evolved than the bulk matrix (Table 2). Therefore, these olivines are antecrysts that were mechanically entrained during the ascent and eruption of the Siwi trachyandesite.

Downloaded from http://petrology.oxfordjournals.org/ by guest on March 22, 2015

Altogether, the major and trace element compositions of the Yasur and Siwi bulk-rocks demonstrate that they belong to a single magmatic series, with different degrees of differentiation. This is especially clear from the positive correlations, passing through zero, between incompatible element pairs (Fig. 3), which define a continuous differentiation trend from the products emplaced during the Yasur explosive activity to the pumices of the Siwi sequence. In contrast, there is an overall decrease of Co (Fig. 3). Long-lived feeding of Tanna volcanism by the same magmatic series is further verified from published data for the Old Tanna ignimbrite (OTI; Robin *et al.*, 1994) and three basalts (Peate *et al.*, 1997) dated at 2·4, 0·67 and 0·23 Ma (Carney & MacFarlane, 1979), which define the least differentiated end-members. In all these samples the correlations between incompatible element pairs are excellent, within the error limits, considering that analyses were performed with different analytical methods and in different laboratories. The regression lines obtained for various element pairs, such as Ba–Th, Rb–Nb and Nb–Th but also Th–Hf, Ta–Th, La–Th, La–Sm and Nb–Y, have high correlation coefficients (Fig. 3; Table 1).

Melt inclusion geochemistry and dissolved volatiles

Yasur distal and proximal products

As representative of Yasur scoria from distal deposits, olivines were systematically hand-picked from 5 fallout layers (TAN 4, 5, 6, 20, 21), with a focus on TAN 6, a sample from the scoria lapilli layer attributed to a violent (sub-Plinian) event. Crystals are commonly elongated in the [100] direction, and display hourglass (skeletal) morphologies that are delineated by small-sized melt inclusions (≤50 μm) and Fe–Ti oxides (Fig. 5a). From experimental work (Faure & Schiano, 2005) we infer that these skeletal textures track the first stage of olivine crystallization. Larger sealed inclusions (≥100 μm), which constitute the most abundant population, and opened glass embayments were trapped during subsequent olivine growth (Fig. 5a). The sealed inclusions are perfectly glassy, with no or only a small shrinkage bubble, which indicates efficient cooling upon magma emplacement. Altogether, melts entrapped in Yasur olivines fall in the compositional domain of the bulk-rocks (Fig. 5b and c) and, therefore, are representative of the carrier magma. The large sealed inclusions and embayments have a very homogeneous composition ($K_2O = 2{\cdot}9$–$3{\cdot}1$ wt %; Table 3) and contain uniform amounts of H_2O (on average 1·07 wt %; $2\sigma/\sqrt{N} = 0{\cdot}05$ with $N = 41$), S (280–350 ppm), Cl (890–920) and F (330–370 ppm). Their S/Cl and Cl/F (wt) ratios average 0·34 and 0·42, respectively. Their CO_2 content varies from 117 to 232 ppm. However, some smaller melt inclusions depart from this chemically homogeneous population in being richer in MgO and poorer in K_2O (≤2·7 wt %; Fig. 5c). They also display higher S (980–680 ppm) and Cl (880–1420 ppm) contents (S/Cl ratio up to 1·0; Fig. 6), whereas their H_2O concentrations (0·8–1·3 wt %) are comparable (Fig. 7).

To complement our melt inclusion study, we systematically analyzed dissolved volatiles in the glassy matrices of the same samples. These glasses are compositionally analogous to the large melt inclusions and glass embayments (Fig. 5). They also preserved comparable amounts of S, Cl and F (Tables 2 and 3), implying their efficient quenching and minor or negligible loss of these volatiles during fast (explosive) magma extrusion. In particular, repeated measurements along 0·5 mm long profiles (11 traverses, ~55 analyses) in vesiculated matrix glasses of sample TAN 4 reveal remarkably constant concentrations of S (130 ± 60 ppm), Cl (870 ± 60 ppm), and F (373 ± 50 ppm), within the error limit (1σ). In contrast, H_2O is largely degassed relative to the melt inclusions and embayments (~0·3 wt % against 1·0–1·2 wt %; Fig. 7). This differing behavior of water with respect to sulfur and halogens is consistent with the much higher diffusivity of water in high-temperature melt (Freda *et al.*, 2005), even during fast magma extrusion.

In proximal scoriae, melt inclusions in olivine (Fo_{67}) and plagioclase ($An_{56–62}$) represent the most evolved trachyandesite terms of the Yasur series, as do their matrix glasses (Fig. 5b and c). There is no significant difference between melt inclusions trapped in either olivine or plagioclase, which points to their negligible evolution after entrapment. All of them are enriched in SiO_2 (~59 wt %) and K_2O (3·7–4·1 wt %), strongly impoverished in H_2O (0·3–0·4 wt %; Fig. 7) and S (<90 ppm), and contain no more detectable CO_2. Their Cl contents (440–590 ppm) and S/Cl ratios (0·1–0·2) are half of those in the distal scoria lapilli (Fig. 6), whereas their F/Cl ratio (0·8–1·0) is twice as high (Table 3). All these features demonstrate extensive degassing of the melt ponding in shallow conduits, during which chlorine is more efficiently released than fluorine. Significant water loss from the inclusions upon magma emplacement is unlikely as the host matrix of these proximal vesicular scoriae is glassy. Instead, these are still more impoverished in H_2O (0·2 wt %), S (<80 ppm, the detection limit), Cl (460 ppm), and partly in F (360 ppm), thereby strongly supporting a pure degassing process.

Systematic optical thermometry measurements on melt inclusions in the Yasur samples reveal a homogeneous temperature of melt entrapment, irrespective of their mineral paragenesis. In distal scoria lapilli (TAN 6), the homogenization temperatures of melt inclusions vary from 1123 to 1093°C in olivine (average 1108 ± 8°C; 11 measurements), and from 1119 to 1104°C (average 1106 ± 6°C; six measurements) in plagioclase. In crater rim scoriae (TAN 12), plagioclase-hosted inclusions homogenize at a very similar mean temperature of 1107 ± 5°C (13 measurements).

Downloaded from http://petrology.oxfordjournals.org/ by guest on March 22, 2015

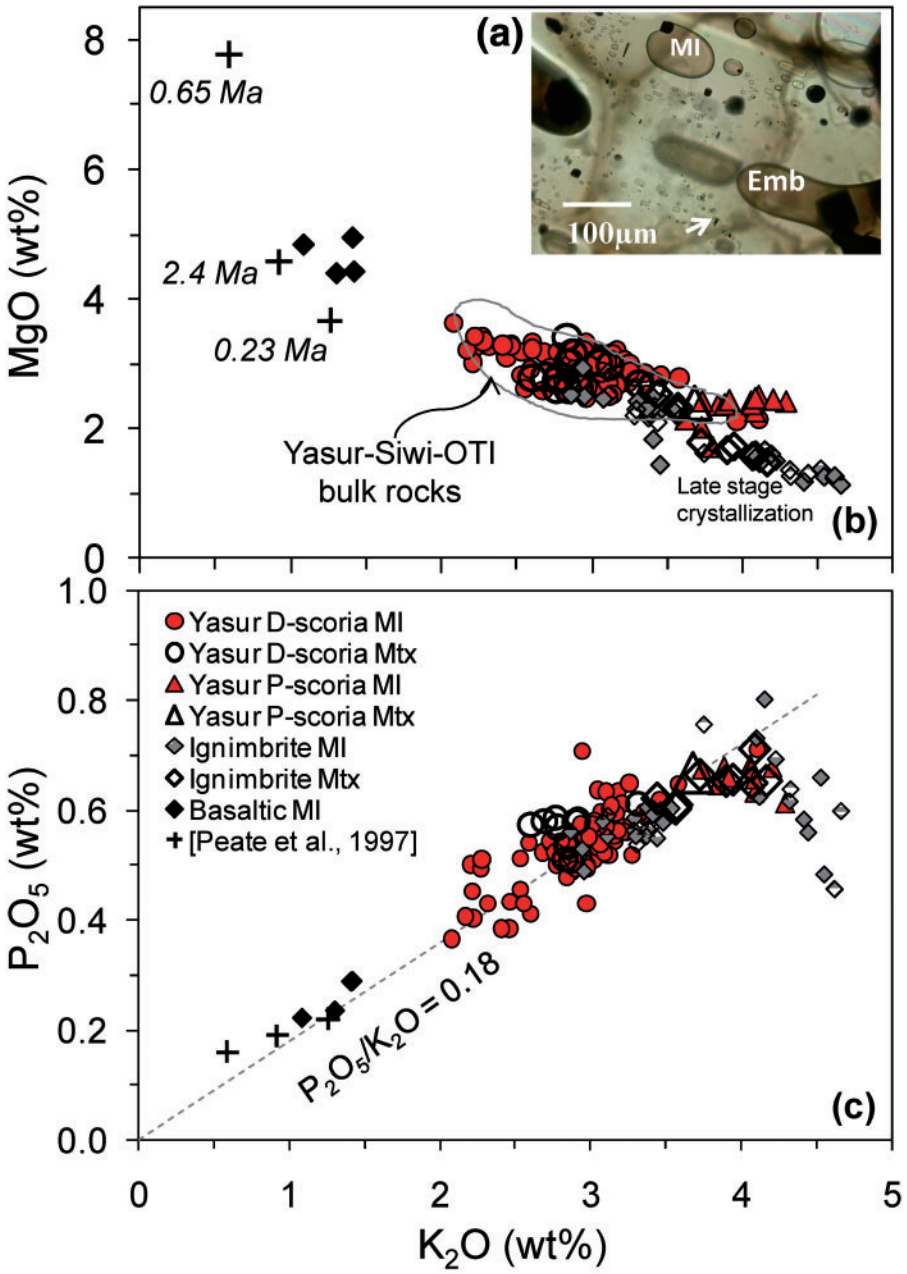

Fig. 5. (a) Transmitted light photomicrograph illustrating the textures of olivines and melt inclusions typical of the Yasur scoria lapilli in distal deposits (TAN 6). Small-sized inclusions delineate, with Fe–Ti oxides, the skeletal texture of the olivine as indicated by the arrow. Large sealed inclusions (MI) and glassy embayments connected with their surroundings (Emb) are indicated. (b, c) Variations of MgO (b) and P_2O_5 (c) as a function of K_2O (wt %) in melt inclusions and glassy matrices of Yasur, and Siwi sequence samples. In addition we have plotted data for Tanna early basalts and basaltic andesites, with their age indicated in italics (data from Peate *et al.*, 1997). D- and P-scoriae stand for distal and proximal scoria products, respectively, which were specifically selected for melt inclusion studies because of their rapid cooling upon emplacement.

Siwi sequence

Pumices of the Siwi sequence provide an interesting series of melt inclusions (Table 4). In basaltic-trachyandesites (samples TAN 1 and 17), melt inclusions hosted in olivine ($Fo_{74–69}$) are compositionally equivalent to or slightly more evolved than those in the Yasur distal samples ($K_2O = 2·9–3·4$ wt %; $P_2O_5/K_2O = 0·18$; Fig. 5b and c). Their S/Cl ratios (~0·2–0·9; Fig. 6), and contents of H_2O (1·1–1·4 wt %; Fig. 7) and CO_2 (<100 to 374 ppm) are also comparable.

Downloaded from http://petrology.oxfordjournals.org/ by guest on March 22, 2015

Table 3: Representative compositions of melt inclusions and open embayments in Yasur distal and proximal products

Sample	MI size (μm)	Bubble	*N*	Host*	SiO_2 (wt %)	TiO_2 (wt %)	Al_2O_3 (wt %)	FeO_{tot} (wt %)	MnO (wt %)	MgO (wt %)	CaO (wt %)	Na_2O (wt %)	K_2O (wt %)	P_2O_5 (wt %)	S (wt %)	Cl (wt %)	F (wt %)	H_2O (wt %)	CO_2 (ppm)	Total	S/Cl	F/Cl
Yasur distal scoriae; open embayments in olivine																						
TAN 6, av.†	≥200	no	28	74·3 (1)	56·21 (30)	0·85 (4)	15·60 (6)	8·56 (15)	0·15 (5)	3·05 (8)	6·11 (9)	3·81 (12)	2·91 (9)	0·51 (1)	0·035 (3)	0·089 (4)	0·037 (15)	1·2 (1)	n.d.	99·11	0·4	0·41
TAN 6, av.	≥200	no	10	73·1 (2)	57·19 (21)	0·83 (2)	15·58 (16)	8·40 (20)	0·17 (2)	2·91 (5)	5·86 (16)	3·82 (2)	3·10 (8)	0·54 (1)	0·032 (1)	0·092 (4)	0·037 (<3)	1·0	202	99·59	0·4	0·40
Yasur distal scoriae; sealed melt inclusions in olivine																						
TAN 6, av.	100–200	no	36	74·2 (3)	56·61 (55)	0·90 (8)	15·67 (18)	8·42 (24)	0·16 (4)	2·92 (10)	5·95 (9)	3·74 (6)	3·04 (13)	0·53 (3)	0·029 (10)	0·091 (3)	0·033 (2)	n.d.	n.d.	98·07	0·31	0·36
TAN 6-25a	100–200	no	3	74·0	56·39	0·87	15·59	8·47	0·12	3·04	5·99	3·75	2·92	0·51	0·035	0·095	n.d.	n.d.	221	97·77	0·36	n.d.
TAN 6-27a	100–200	no	3	74·2	57·09	0·93	15·55	8·35	0·16	3·05	5·60	3·78	2·89	0·56	0·018	0·088	0·033	n.d.	117	98·09	0·21	0·38
TAN 6-32	100 × 70	yes	4	74·6	56·32	0·84	15·68	8·61	0·13	3·16	6·28	3·69	2·68	0·52	0·027	0·085	0·040	1·2	n.d.	99·24	0·3	0·47
TAN 6-39a	100 × 60	no	2	75·2	56·00	1·03	15·83	8·25	0·20	3·11	6·33	3·67	3·18	0·64	0·014	0·110	n.d.	1·3	n.d.	99·66	0·1	n.d.
TAN 6-39b	40 × 50	no	2	74·9	56·96	0·91	15·62	8·34	0·09	3·00	6·07	3·60	3·12	0·58	0·011	0·101	n.d.	1·1	n.d.	99·53	0·1	n.d.
TAN 6-41a	25 × 25	no	2	74·4	55·72	0·84	15·56	9·29	0·26	3·30	6·55	3·74	2·47	0·43	0·075	0·123	n.d.	0·9	n.d.	99·27	0·6	n.d.
TAN 6-41b	90 × 80	no	3	74·4	56·74	0·80	15·69	9·03	0·15	3·18	6·49	3·71	2·53	0·45	0·076	0·129	n.d.	0·9	n.d.	99·85	0·6	n.d.
TAN 6-43	25 × 26	no	3	74·9	55·83	0·64	15·72	9·36	0·13	3·24	7·09	3·65	2·22	0·40	0·088	0·106	n.d.	1·3	n.d.	99·77	0·8	n.d.
TAN 6-45	30 × 40	yes	3	74·1	56·23	0·95	15·34	8·98	0·14	3·14	6·32	3·67	2·84	0·48	0·136	0·171	n.d.	1·0	n.d.	99·39	0·8	n.d.
TAN 6-50a	90 × 80	no	4	72·7	56·26	0·65	15·59	9·46	0·22	3·27	7·16	3·75	2·32	0·43	0·078	0·097	n.d.	0·8	n.d.	100·11	0·8	n.d.
TAN 6-ir2a	30 × 40	yes	2	74·8	56·10	0·97	15·48	8·33	0·14	3·16	5·84	3·85	3·07	0·60	0·013	0·102	n.d.	1·0	n.d.	98·67	0·1	n.d.
TAN 6-30	180 × 220	yes	4	74·9	53·64	0·64	16·23	9·44	0·22	3·64	7·82	3·56	2·08	0·37	0·090	0·088	n.d.	1·1	89	98·62	1·0	n.d.
TAN 6-34a	100 × 140	yes	3	73·1	56·41	0·87	15·96	8·66	0·16	2·88	6·32	3·55	2·85	0·54	0·017	0·075	0·023	0·9	30‡	99·25	0·2	0·3
TAN 6-29a	30 × 40	yes	3	n.d.	54·27	1·03	15·86	9·45	0·15	3·00	6·56	3·58	2·78	0·53	0·081	0·106	n.d.	1·1	n.d.	98·47	0·8	n.d.
TAN 6-24a	30 × 40	yes	2	72·8	53·15	0·67	16·51	10·01	0·15	2·82	7·04	3·90	2·53	0·51	0·333	0·263	n.d.	n.d.	n.d.	97·90	1·3	n.d.
TAN 5-4	80 × 60	yes	4	75·1	55·49	0·61	15·56	8·82	0·20	3·43	6·68	4·16	2·22	0·45	0·098	0·095	n.d.	n.d.	n.d.	97·81	1·0	n.d.
TAN 20-6,10	50 × 60	no	5	71·7	57·61	0·93	15·60	8·68	0·17	2·82	5·73	3·78	3·33	0·61	0·020	0·091	n.d.	n.d.	n.d.	99·37	0·2	n.d.
Yasur proximal scoriae; melt inclusions in olivine																						
TAN 12-8	30 × 25	no	3	67·2	59·26	0·80	14·88	8·24	0·21	1·72	5·31	3·73	3·80	0·68	0·006	0·055	n.d.	0·4	n.d.	99·06	0·1	n.d.
TAN 12-4a	40 × 50	no	2	67·2	59·08	1·00	14·93	8·50	0·19	2·02	5·56	3·65	3·73	0·70	0·009	0·055	n.d.	n.d.	n.d.	99·42	0·2	n.d.
TAN 12-4b	40 × 50	no	3	67·2	58·97	0·97	14·93	8·66	0·11	2·14	5·43	3·67	3·62	0·67	0·009	0·059	n.d.	0·4	n.d.	99·67	0·1	n.d.
Yasur proximal scoriae; melt inclusions in plagioclase																						
TAN 12-1a	120 × 90	no	4	56·4	59·24	0·99	14·68	8·31	0·20	2·36	4·86	3·64	3·84	0·65	0·009	0·046	0·045	0·3	n.d.	99·20	0·2	1·0
TAN 12-1b	70 × 50	no	2	55·7	59·34	1·02	14·66	7·99	0·23	2·27	4·52	3·54	4·09	0·63	0·006	0·044	n.d.	0·4	n.d.	98·72	0·1	n.d.
TAN 12-6a	200 × 70	no	3	62·4	58·86	0·98	14·65	8·50	0·16	2·43	5·08	3·48	3·74	0·67	0·008	0·048	0·039	n.d.	n.d.	98·64	0·2	0·82
TAN 12-10	60 × 40	no	3	57·5	58·85	0·97	14·50	8·60	0·16	2·44	4·72	3·45	3·92	0·66	0·006	0·053	n.d.	0·4	n.d.	98·71	0·1	n.d.

N, number of analyses in one or several melt inclusion(s) (MI). n.d., not determined.
*Composition of the host mineral expressed in Fo mol % [100Mg/(Mg + Fe)] for olivine and An mol % [100Ca/(Ca + Na + K)] for plagioclase.
†Averaged analyses of melt inclusions and embayments entrapped in several crystals, with standard deviations given in parentheses [i.e. (1) for 0·51 ± 0·01].
‡Below detection limit.

Downloaded from http://petrology.oxfordjournals.org/ by guest on March 22, 2015

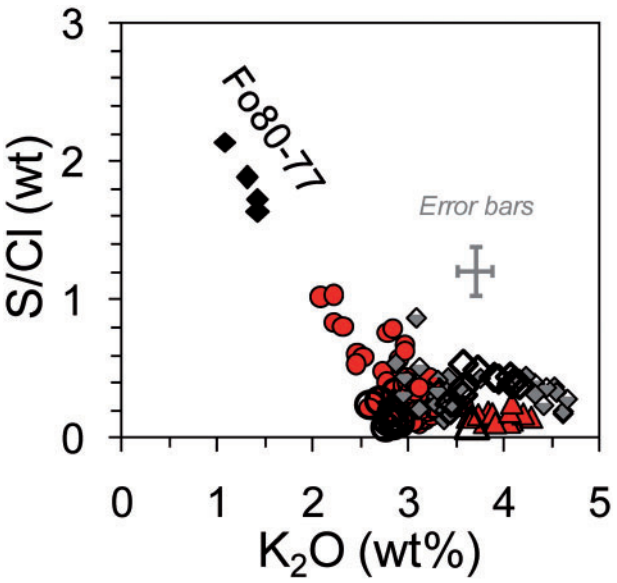

Fig. 6. Variations of the S/Cl (wt ratio) vs K_2O (wt %) in melt inclusions, embayments and glassy matrices of Yasur and Siwi sequence products. Symbols as in Fig. 5.

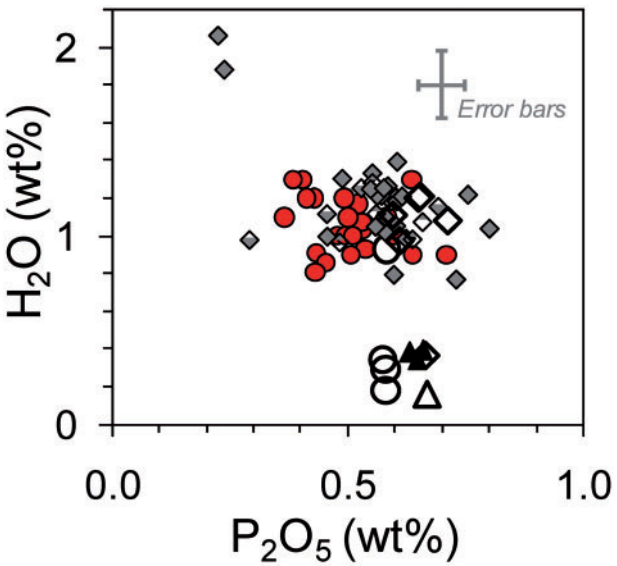

Fig. 7. Variations of H_2O (wt %) as a function of P_2O_5 (wt %) in melt inclusions, embayments and glassy matrices of Yasur and Siwi products. Symbols as in Fig. 5.

In the trachyandesite (TAN 23), melt inclusions trapped in Fe-rich olivines, plagioclase, clinopyroxene and apatite display the most evolved compositions (Fig. 5b and c). They are even more evolved than the surrounding matrix, which indicates local melt evolution during crystallization of the four mineral phases (P_2O_5 depletion being due to apatite formation). These inclusions contain ~180 ppm of CO_2, and 1·1 wt % of H_2O on average (Fig. 7). They are partially degassed with respect to S (220–360 ppm) and Cl (690–840 ppm), but to about a same extent as the embedding matrix glasses (Table 2). The same observation applies to the less evolved and less degassed matrix glasses of the Siwi basaltic-trachyandesites, whose S and Cl contents do not differ much from those in the melt inclusions.

Most importantly, we find that the few Mg-rich ($Fo_{77–80}$) olivine antecrysts present in the Siwi trachyandesite have entrapped melt inclusions with a basaltic composition, comparable with that of the bulk Tanna basalts (Fig. 5b and c). These inclusions are the richest in CaO (up to 10 wt %; CaO/Al_2O_3 up to 0·59) and the poorest in P_2O_5 and K_2O ($P_2O_5/K_2O = 0·18$; Fig. 5c), once corrected for the limited effect of post-entrapment crystallization of their host (Table 4). They represent the least evolved melt of the Yasur–Siwi magmatic series, and thus provide unique information on the volatile content of the parental basaltic magma of Tanna volcanism. These scarce basaltic inclusions contain between 1 and 2 wt % of H_2O (Fig. 7), 1000 ppm of S (without any immiscible sulfide globules), and 550 ppm of Cl ($S/Cl = 1·8 \pm 0·2$; Fig. 6). Their CO_2 content ranges from 573 to 130 ppm, without co-varying with H_2O. However, they also contain bubbles into which carbon dioxide could have migrated upon cooling after entrapment. Consequently, their dissolved CO_2 content may represent a lower limit for the amount of that species at the time of melt entrapment.

YASUR VOLCANIC GAS EMISSIONS

Gas composition

Figure 8 shows the temporal variations of SO_2 and air-corrected CO_2 and H_2O concentrations in Yasur volcanic gas emissions, as recorded on 21 October 2007. In the first ~22 min enhanced plume condensation prevented H_2O retrieval. The observed variations are due to both the pulsed explosive activity and variable air dilution of the volcanic plume during the interval of measurement. Looking at the relative behavior of the volatile species, however, reveals a very coherent pattern for CO_2 and SO_2. The best-fit regression line in a scatter plot of CO_2 vs SO_2 concentrations (Fig. 9a) constrains a mean CO_2/SO_2 molar ratio of $1·6 \pm 0·4$ (Table 5), with minor and short-lived temporary fluctuations (from <1·5 to >3). A comparable CO_2/SO_2 mean ratio (1·8–2; Table 5) was measured on 29–30 October, and had previously been reported (~2·0) from Fourier transfor infrared (FTIR) remote sensing in 2005 (Oppenheimer *et al.*, 2006). This parameter thus appears to be rather steady in Yasur volcanic gas emissions. In fact, Oppenheimer *et al.* (2006) reported no difference in CO_2/SO_2 ratio during quiescent and explosive degassing in 2005, in sharp contrast to observations

Downloaded from http://petrology.oxfordjournals.org/ by guest on March 22, 2015

Table 4: Representative compositions of melt inclusions in pumices of Siwi ignimbrite

Sample	MI size (μm)	Bubble	*N*	Host*	SiO_2 (wt %)	TiO_2 (wt %)	Al_2O_3 (wt %)	FeO_{tot} (wt %)	MnO (wt %)	MgO (wt %)	CaO (wt %)	Na_2O (wt %)	K_2O (wt %)	P_2O_5 (wt %)	S (wt %)	Cl (wt %)	H_2O (wt %)	CO_2 wt ppm	Total	S/Cl
TAN 1 and 17; melt inclusions in olivine																				
TAN 1-4	75 × 50	no	3	71·2	58·43	0·76	15·46	7·92	0·20	2·35	5·11	3·92	3·40	0·59	0·019	0·089	1·2	94	99·44	0·2
TAN 1-8a	70 × 80	yes	3	69·2	57·80	0·97	15·49	8·25	0·22	2·46	5·45	4·33	3·08	0·58	0·068	0·078	1·1	128	99·87	0·9
TAN 1-11b	60 × 90	no	3	74·4	56·38	0·97	15·76	8·52	0·14	2·95	6·13	3·69	2·94	0·53	0·026	0·084	1·3	323	99·35	0·3
TAN 1-12	60 × 40	no	3	69·3	58·27	0·82	15·48	7·97	0·18	2·21	5·20	3·99	3·39	0·60	0·020	0·087	1·2	287	99·38	0·2
TAN 1-19a	100 × 50	no	5	70·8	57·44	0·85	15·75	7·80	0·15	2·35	5·35	4·03	3·37	0·60	0·019	0·080	1·4	48[c]	99·17	0·2
TAN 17-1b	100 × 50	no	3	72·5	57·67	0·83	16·03	7·62	0·14	2·29	6·05	3·96	3·30	0·55	0·032	0·092	1·3	374	99·84	0·3
TAN 23; basaltic melt inclusions in olivine																				
TAN 23-18	60 × 80	yes	3	79·4	49·53	0·72	16·94	9·03	0·20	4·85	10·04	3·22	1·09	0·22	0·100	0·047	2·1	133	98·04	2·1
TAN 23-26	60 × 50	yes	3	79·7	48·68	1·11	18·84	8·28	0·02	4·43	10·60	3·67	1·42	0·29	0·100	0·061	1·0	573	98·48	1·6
TAN 23-3	60 × 50	yes	3	80·4	49·68	0·68	17·36	8·70	0·11	4·95	9·42	3·29	1·42	0·29	0·100	0·058	n.d.	n.d.	96·05	1·7
TAN 23-27b	200 × 150	yes	3	76·7	49·50	0·67	17·65	9·63	0·15	4·40	9·70	3·39	1·31	0·24	0·096	0·051	1·9	n.d.	98·66	1·9
TAN 23; evolved melt inclusions																				
TAN 23-4 ol	40 × 70	Sulfide	3	58·5	61·52	0·78	14·54	6·85	0·16	1·36	3·32	4·00	4·52	0·66	0·0247	0·0672	1·1	107	98·89	0·4
TAN 23-6 ol	80 × 90	yes	3	58·9	61·40	0·83	14·68	6·91	0·12	1·35	3·26	4·05	4·32	0·62	0·0268	0·0682	1·2	240	98·85	0·4
TAN 23-8 ol	50 × 40	Sulfide	3	59·3	61·90	0·74	14·59	6·33	0·19	1·25	3·19	4·01	4·54	0·48	0·0213	0·0647	1·0	196	98·28	0·3
TAN 23-19b ol	50 × 30	no	3	58·1	62·30	0·84	14·84	6·69	0·15	1·22	3·09	4·16	4·61	0·46	0·0117	0·0670	1·0	n.d.	99·43	0·2
TAN 23-19a ol	25 × 40	no	3	59·0	62·46	0·81	14·82	6·60	0·20	1·26	2·95	4·22	4·61	0·46	0·0133	0·0703	1·1	n.d.	99·57	0·2
TAN 23-12a ol	70 × 50	Sulfide	3	57·2	61·85	0·82	15·09	7·34	0·15	1·30	3·28	4·14	4·44	0·56	0·0273	0·0753	1·0	n.d.	100·11	0·4
TAN 23-Plagio	60 × 50	yes	4	53·6	59·16	0·90	15·36	7·30	0·26	1·66	3·91	4·12	4·15	0·80	0·036	0·084	1·0	n.d.	98·77	0·4
TAN 23-Cpx	30 × 40	Sulfide	4	21·6	61·37	0·87	14·60	6·92	0·14	1·36	3·54	4·28	4·22	0·63	0·026	0·074	1·0	n.d.	99·01	0·4
TAN 23-Apat	30 × 100	Sulfide	4	F-apat.	59·60	0·80	14·64	8·02	0·21	1·62	4·42	3·95	3·75	0·76	0·034	0·079	1·2	n.d.	99·10	0·4

Inclusions are in equilibrium with their hosts, except those in olivine Fo_{77-80}, which were corrected for post-entrapment olivine crystallization, given fO_2 buffered at NNO and a K_D value of 0·30. *N*, number of analyses in one or several melt inclusion(s) (MI). Apatite included in plagioclase and clinopyroxene is a fluoroapatite (F = 2·15 ± 0·15; Cl = 0·59 ± 0·01), coexisting with Cu-rich sulfide ($Cu_{0·67}$, $Fe_{0·48}$, $S_{0·91}$).
*Composition of the host mineral expressed in Fo mol % [100Mg/(Mg + Fe)] for olivine, An mol % [100Ca/(Ca + Na + K)] for plagioclase and Fs mol % [100Fe/(Ca + Mg + Fe)] for pyroxene.

Downloaded from http://petrology.oxfordjournals.org/ by guest on March 22, 2015

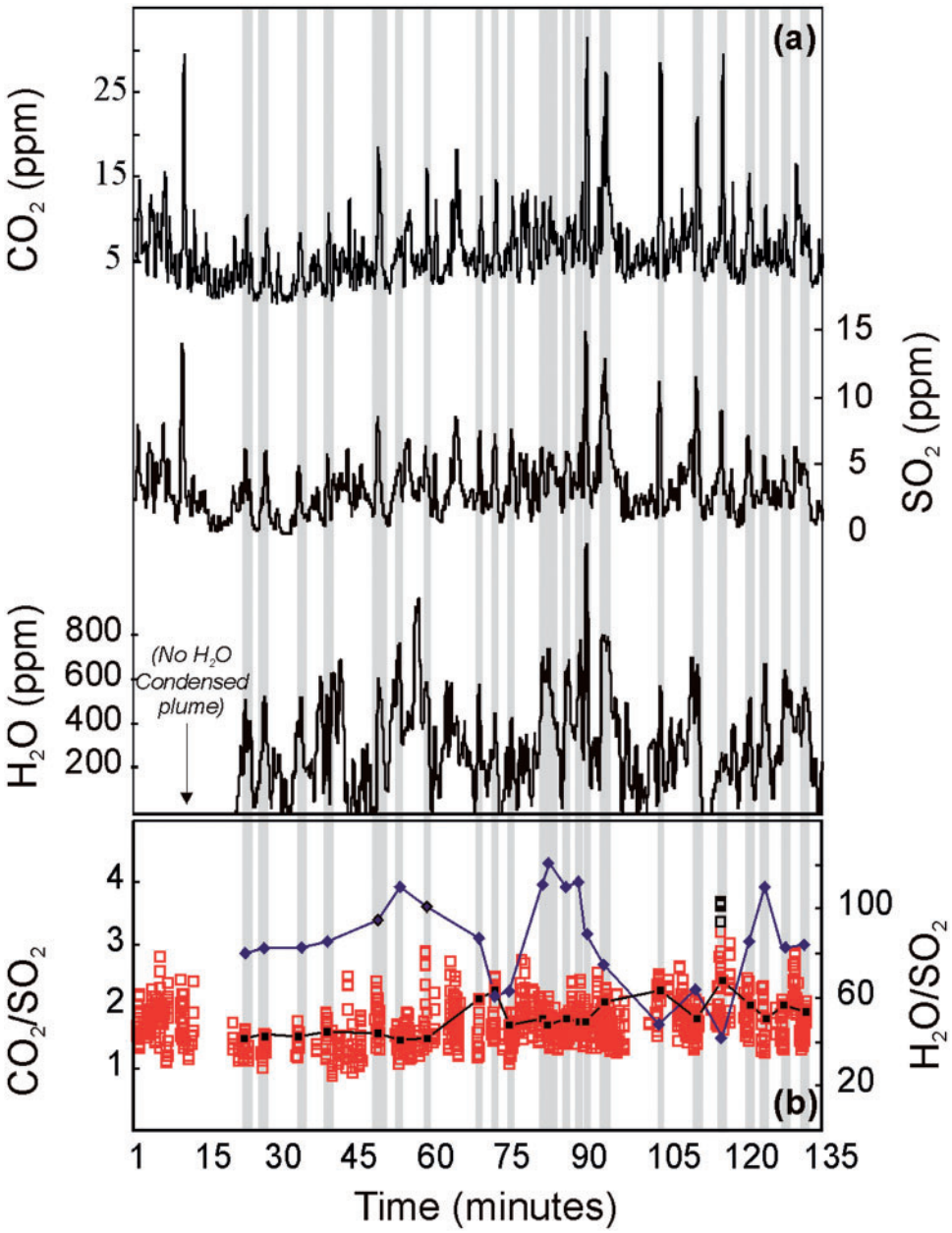

Fig. 8. (a) Time record of CO_2, SO_2 and H_2O concentrations (in ppm) in the Yasur plume on 21 October 2007. For CO_2 and H_2O, we report in-plume concentrations after subtraction of background air contents (384–387 ppm and 19440–21020 ppm for CO_2 and H_2O, respectively). (b) Time record of CO_2/SO_2 and H_2O/SO_2 molar ratios in the Yasur plume. Open squares, high-rate record of CO_2/SO_2 ratios, calculated by taking the point-to-point ratio of CO_2 and SO_2 concentrations reported in (a) (the ratios were calculated for all the couples of MultiGas measurements for which SO_2 concentration was above the threshold value of 2 ppm); black filled squares, mean CO_2/SO_2 ratios calculated from subsets of CO_2 and SO_2 concentrations acquired within the same time intervals used above for H_2O/SO_2 ratios (ratios calculated as described above for H_2O/SO_2); diamonds, mean H_2O/SO_2 ratios calculated from subsets of H_2O and SO_2 concentrations acquired within specific time intervals. These time windows (indicated by the vertical grey bars) were selected as those showing the highest H_2O air-corrected concentrations and peak SO_2 concentrations >5 ppm. The mean H_2O/SO_2 ratios were calculated by drawing, for each time window, a SO_2 vs H_2O scatter diagram, and calculating the corresponding ratio from the slope of the best-fit regression line.

during analogous activity at Stromboli volcano, in Italy (Burton *et al.*, 2007).

The relative behavior of H_2O vs SO_2 is much more variable (Fig. 9b and c), owing to the inherent complexity in resolving volcanic H_2O from the high and changing air humidity background on top of Yasur. The volcanic H_2O/SO_2 molar ratio was thus assessed by considering only the time windows during which highest SO_2 and air-corrected

Downloaded from http://petrology.oxfordjournals.org/ by guest on March 22, 2015

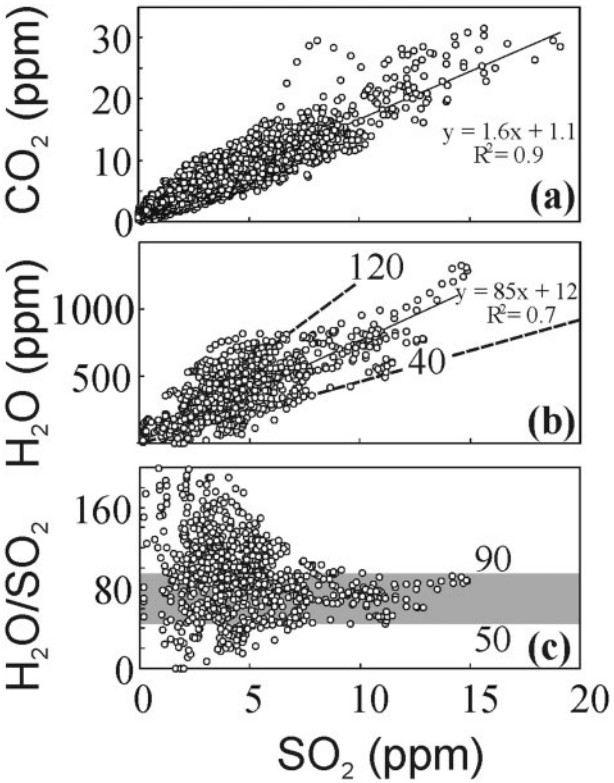

Fig. 9. (a) Scatter diagram of MultiGas-sensed SO_2 and CO_2 concentrations (in ppm), including the entire dataset of Fig. 8a. The mean plume CO_2/SO_2 ratio of 1·6 is derived from the slope of the best-fit regression line (see Shinohara *et al.*, 2008; Aiuppa *et al.*, 2007, for more details). (b) Scatter diagram of MultiGas-sensed SO_2 and H_2O concentrations (in ppm), drawn from data acquired within the selected time intervals indicated as grey bars in Fig. 8. (c) Scatter diagram of SO_2 concentrations (in ppm) against the plume H_2O/SO_2 ratios. The diagram shows that as plume density (and therefore SO_2 concentration) increases the spread of observed H_2O/SO_2 ratios becomes narrower. The H_2O/SO_2 ratio range of 50–90 (on average 70) is therefore accepted as the most representative of Yasur gas emissions.

H_2O concentrations were recorded on 21 October (grey vertical bars in Fig. 8). Although it varied widely even during these intervals (from 40 to 120; Fig. 9b), the H_2O/SO_2 ratio was more restricted (from 50 to 90) when the volcanic plume was more concentrated (>5 ppm SO_2; Fig. 9c). Although the lower values may be more representative (given the plume dilution factor of order 10^2–10^3), we considered here the mean volcanic H_2O/SO_2 molar ratio of 70 ± 20. Measurements on 29–30 October gave higher and even more variable ratios (120 ± 60 and 160 ± 60, respectively; Table 5), which, as mentioned above, were affected by a higher and more erratic moisture air background. It should be noted that H_2O could not be determined with FTIR remote sensing at Yasur in 2005 (Oppenheimer *et al.*, 2006) and so our results are the first for this volcano.

Chemical analysis of filter pack samples demonstrates reasonable stability of the volcanic HCl/SO_2 (0·33–0·53) and HF/SO_2 (0·095–0·12) molar ratios during our 21 and 29–30 October surveys (Table 5 and Fig. 10). It should be noted that these ratios characterize the time-integrated emission during both passive and explosive magma degassing. This prevented us from detecting the sharp SO_2/HCl peak increases (up to 30) during single explosions that were measured with remote FTIR sensing at Yasur in 2005 (Oppenheimer *et al.*, 2006), and in 2008 (Allard *et al.*, in preparation). However, the average SO_2/HCl molar ratio of $2{\cdot}4 \pm 0{\cdot}4$ derived from our measurements does not differ much from the mean SO_2/HCl molar ratio (~2·0) for purely passive degassing reported by Oppenheimer *et al.* (2006), which means that passive gas emissions supply a prevalent fraction of the overall Yasur gas budget.

Combining our results from both MultiGas and filter-pack measurements, and normalizing to 100%, we derive the mean composition for Yasur volcanic gases reported in Table 5. As verified from MultiGas sensing on 29–30 October, the contribution of other gas species such as H_2S and H_2 is minor ($H_2S/SO_2 < 0{\cdot}01$ and $H_2/SO_2 < 0{\cdot}1$). Yasur gas emissions thus appear to be highly hydrous (~98 mol % H_2O) and oxidized (SO_2/H_2S ratio >100); these are typical features for magmatic gas emissions from arc volcanoes worldwide (e.g. Symonds *et al.*, 1994). Their CO_2 content is relatively modest and their HCl/HF molar ratio (~4) ranks among the lowest ratios measured at arc volcanoes (1·9–160; Aiuppa, 2009).

Gas fluxes

The SO_2 column amounts measured during our DOAS traverses beneath the Yasur volcanic plume occasionally displayed up to three peaks, tracking gas emission from the three active vents in the crater. The mean SO_2 fluxes determined on 20–21 and 29–30 October 2007 are 940 and 620 tons per day (tons d^{-1}), respectively (Electronic Appendix 2). Their average (690 ± 330 tons d^{-1}) is identical to the time-averaged SO_2 flux of 680 ± 380 tons d^{-1} constrained by repeated measurements at Yasur in 2004–2009 (Bani & Lardy, 2007; Bani *et al.*, in preparation). Therefore, our gas results in October 2007 are representative for the standard eruptive activity of the volcano.

Combining the chemical composition of the volcanic gas with the measured SO_2 fluxes, we directly derive the emission rate of the other volatile species (Table 5). The daily mean fluxes (tons d^{-1}) are in the range of $13{\cdot}4 \times 10^3$ for H_2O, 840 for CO_2, 165 for HCl and 23 for HF. The total gas flux, quantified here for the first time, averages $\sim 15 \times 10^3$ tons d^{-1}. According to these results, Yasur volcano ranks among typical arc emitters: it contributes *c.* 1·7–1·9% of global volcanic emissions of H_2O ($\sim 8 \times 10^5$ tons d^{-1}; Wallace, 2005), and SO_2 ($\sim 3{\cdot}6 \times 10^4$ tons d^{-1}; Andres & Kasgnoc, 1998), ~0·3–2·4% of global CO_2

Downloaded from http://petrology.oxfordjournals.org/ by guest on March 22, 2015

Table 5: Chemical compositions and mass fluxes of Yasur crater gas emissions

Date:	10/21/2007	10/29/2007	10/30/2007	Mean ratios	Jan. 2005*
H_2O/SO_2	50–90	120 ± 60	160 ± 60	70 ± 20	n.d.
CO_2/SO_2	1·6 ± 0·4	1·8 ± 0·5	2·0 ± 0·5	1·8 ± 0·2	2·0
HCl/SO_2	0·33 ± 0·08	0·53 ± 0·10	0·44 ± 0·06	0·43 ± 0·10	0·5
HF/SO_2	0·12 ± 0·035	0·095 ± 0·031	0·12 ± 0·014	0·11 ± 0·01	n.d.
HCl/HF	2·8	5·6	3·7	4·0 ± 1·4	n.d.

	Recalculated compositions and gas flux estimates						
	mol %	Mg d^{-1}	mol %	Mg d^{-1}	mol %	Mean fluxes†	Mg d^{-1}
H_2O	97	13220–23790	97	20900	98	13390	–
CO_2	1·8	1030	1·5	770	1·2	840	1330
SO_2	1·1	940	0·8	620	0·6	680	970
HCl	0·38	177	0·43	187	0·27	164	276
HF	0·14	35	0·08	18	0·07	23	–
Total						15097	

*S/Cl ratio during quiescent degassing, difference between passive and explosive not resolved for CO_2 (CO_2/SO_2; Oppenheimer *et al.*, 2006).
†Mean fluxes are the 2007 mean gas fluxes (H_2O, CO_2, HCl, HF) calculated for a time-averaged SO_2 flux of 680 tons d^{-1} (Bani & Lardy, 2007).

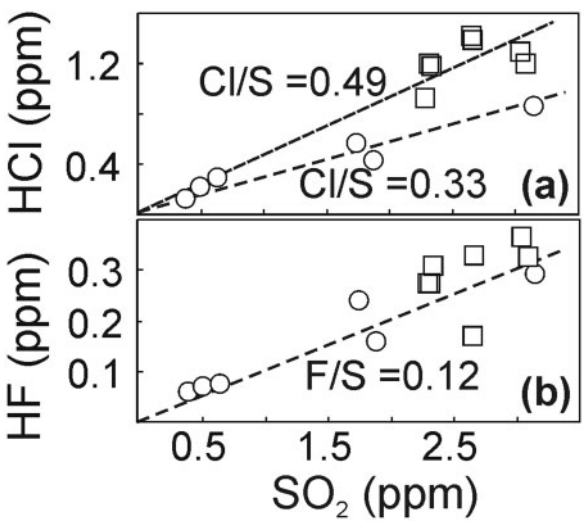

Fig. 10. Scatter diagrams of (a) HCl vs SO_2 and (b) HF vs SO_2 in-plume concentrations, derived from filter-pack measurements. These data should be viewed as time-integrated plume concentrations over the filter-pack sampling intervals (ranging from 45 to 60 min). Circles, 21 October samples; squares, 29–30 October samples.

emissions ($0{\cdot}4$–$3{\cdot}5 \times 10^5$ tons d^{-1}; Arthur, 2000), ~1·4% of HCl (~$1{\cdot}2 \times 10^4$ tons d^{-1}; Pyle & Mather, 2009), and 0·5% of HF (~5×10^3 tons d^{-1}; Pyle & Mather, 2009). However, its volatile source strength is an order of magnitude lower than that of nearby Ambrym volcano, in the central Vanuatu arc (Allard *et al.*, 2009; Bani *et al.*, 2009).

DISCUSSION

Long-term feeding of Tanna volcanism by the same arc basalt

We show here that the Yasur–Siwi magmas belong to the same magmatic evolution series as both the Old Tanna Ignimbrite (OTI; Robin *et al.*, 1994) and Tanna basalts erupted as long as 2·4 Myr ago (Carney & MacFarlane, 1979; Peate *et al.*, 1997). This conclusion, deduced from both major and trace elements (Fig. 3) in the bulk-rocks, is also verified by the composition of melt inclusions: these cover a complete range from basalt—comparable with bulk Tanna basalts—to the most evolved trachyandesite erupted during the Siwi ignimbrite eruption (Fig. 5b and c). Hence, we propose that a geochemically homogeneous basaltic magma could have supplied Tanna volcanism for ~2 Myr.

Furthermore, our study demonstrates that basaltic-trachyandesites erupted during the last 1400 years of volcanic activity in the Siwi caldera have maintained a constant bulk composition, in agreement with previous observations by Nairn *et al.* (1988). Such a constancy points to steady conditions of magma supply and differentiation

Downloaded from http://petrology.oxfordjournals.org/ by guest on March 22, 2015

during this time interval. We did not find any textural or mineralogical evidence of basalt input and mixing with more evolved trachyandesitic magmas in the Yasur–Siwi products (Figs 3 and 5). This conclusion is also supported by the S and Cl behavior, as discussed below. Robin *et al.* (1994) made the same observation for the OTI and Siwi deposits. Therefore, crystal fractionation is the dominant process controlling basalt differentiation towards the compositions of the Yasur and Siwi magmas, even though mixing between cogenetic melts that have differentiated along the same liquid line of descent cannot be totally excluded. Based on their average bulk Th (1·9 ppm) and Nb (1·1 ppm) contents, we compute that Yasur basaltic-trachyandesites derive from a basaltic parent magma (Th = 0·9 ppm, Nb = 0·6 ppm) by ~50% crystal fractionation (removal). The generation of the most evolved trachyandesitic magma (Th = 3·3 ppm) extruded during the Siwi ignimbrite eruption (TAN 23 and 24), requires a higher extent (≥70%) of differentiation.

The Yasur–Siwi magma series displays high U/Nb (1 ± 0·1) and Th/Ta (23 ± 1) ratios typical for a subduction context, and La/Yb ratios (5·7 ± 0·3) that are similar to those for island arc basalts in the southern Vanuatu arc (Monzier *et al.*, 1997). Following Peate *et al.* (1997), their overall enrichment in Ba and K, together with their low Zr/Yb (43 ± 2) and Nb/Yb (0·53 ± 0·02) ratios, points to the contribution of slab-derived fluids to a depleted MORB-mantle source. The high Th/Nb ratio (1·7) could be compatible with the involvement of a sediment-derived component (Johnson & Plank, 1999; Elliott, 2003), as also inferred for other Vanuatu lavas (Peate *et al.*, 1997). Alternatively, these trace element ratios could be controlled by the stability of accessory phases in the subducting slab (Skora & Blundy, 2010). Sediments subducted beneath Tanna, which derive from the North Loyalty Basin, are prevalently composed of andesitic–dacitic volcano-clastic debris associated with silt–sandstone and conglomerate horizons, ash units rich in nanofossils, radiolaria and clays (e.g. Peate *et al.*, 1997). Such sediments can be expected to contribute a small amount of volatiles to the mantle wedge upon subduction, in agreement with our finding of modest volatile enrichment of the Tanna parental basalts.

According to our data for the most primitive melt inclusions in Mg-rich olivines, the parental basalt of the Siwi–Yasur magma series is moderately hydrous (1–2 wt % H_2O), weakly enriched in sulfur (~0·1 wt %), and rather poor in Cl (~0·055 wt %). In fact, it falls within the domain for Cl-poor arc magmas whose genesis requires the contribution of ≤5 wt % slab-derived equivalent NaCl to a MORB-mantle source (Wallace, 2005). The low Cl content of this basalt is also consistent with the low HCl/HF molar ratio (2·8–5·6) of Yasur gas emissions compared with other arc volcanic gases (1·9–160; Aiuppa, 2009). Moreover, Yasur melts, with an average Cl/H_2O wt ratio ≤0·05, are far from being saturated with a hydrous saline liquid (Webster *et al.*, 1999). Finally, the relatively low CO_2/SO_2 ratio of Yasur arc volcanic gases, the modest CO_2 emission rate (~840 tons d^{-1} on average) and the rather low dissolved CO_2 content of local thermal waters (Gauthier *et al.*, in preparation), all concur to suggest a moderate enrichment of the parental basalt in carbon dioxide.

Depths and conditions of magma differentiation

The depths and conditions of magma differentiation beneath Siwi caldera were assessed from both our melt inclusion data and MELTS calculations (Ghiorso & Sack, 1995). Assuming volatile saturation, the dissolved CO_2 and H_2O contents of olivine-hosted melt inclusions in the Yasur–Siwi lavas allow us to estimate the total fluid pressures ($P_{CO2} + P_{H2O}$) and, hence, the lithostatic depth at the time of entrapment of the various liquids (Electronic Appendix 3). For these calculations we used the solubility model of Papale *et al.* (2006), taking account of the fact that CO_2 solubility data are still poorly documented for basaltic-trachyandesite compositions. Melt temperatures were derived from MELTS computations and from our thermometry measurements. Finally, redox conditions close to the nickel–nickel oxide (NNO) buffer were found to best fit with the composition and mineralogy of the Yasur–Siwi magmas (see below) and, hence, were used in our calculations.

Parental basalt

For the basalt, accurate pressure estimates are hampered by the scarcity of our data for the basaltic melt inclusions and their variability in both CO_2 (from 574 to 103 ppm) and H_2O (from 1 to 2 wt %). Moreover, the measured dissolved CO_2 contents may represent lower limits, as mentioned above. For the most CO_2-rich inclusion, with 1 wt % H_2O, we infer a minimal entrapment pressure of 155 MPa (Fig. 11, and Electronic Appendix 3), corresponding to ~6 km lithostatic depth for a mean host-rock density of 2700 kg m^{-3}. Alternatively, one can place an upper limit on the initial CO_2 content and saturation pressure of the basalt from its pre-eruptive S content of 0·1 wt % and the CO_2/SO_2 ratio of Yasur gas emissions (1·6–2·0; Table 5). From these parameters we compute a total (dissolved and exsolved) amount of ~0·22–0·27 wt % CO_2 in the basaltic system, which, if originally dissolved together with 1–2 wt % H_2O, would imply volatile saturation at ~290–330 MPa or ~11–12 km lithostatic depth under NNO redox conditions. It should be noted that such an amount is rather modest when compared with that of basaltic arc melts stored at crustal depths, which typically contain 0·2 to <0·5 wt % of dissolved CO_2 but also coexist with an exsolved CO_2-rich gas phase (e.g. Wallace, 2005).

Downloaded from http://petrology.oxfordjournals.org/ by guest on March 22, 2015

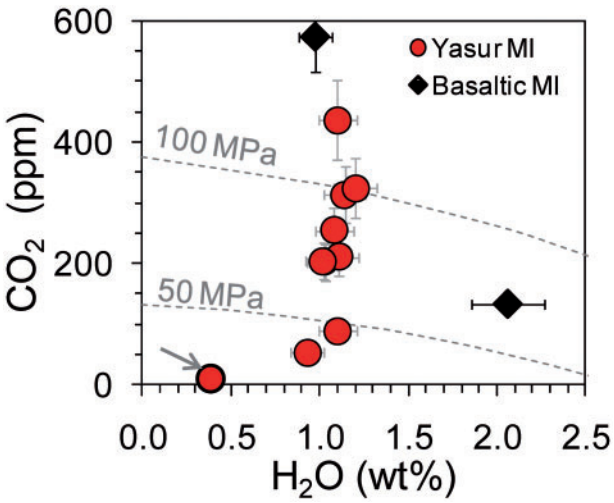

Fig. 11. Pressure-related variation of CO_2 and H_2O in olivine-hosted melt inclusions (MI) of Yasur distal scoria lapilli and in two basaltic melt inclusions. The arrow indicates the mean composition of the melt inclusions in scoriae emplaced on the crater rim representative of the degassed and crystallized magma stored in the upper parts of the conduit.

This is again consistent with the idea of minor carbon recycling beneath the southern Vanuatu arc.

MELTS calculations must be considered with caution as they do not include the effect of CO_2 on the stability field of the mineral phases (Ghiorso & Sack, 1995). However, water exerts the main influence on the crystallization path of magmas that are weakly or moderately enriched in carbon dioxide, such as inferred here for the Tanna basalt. Our MELTS computations, performed at between 1150 and 1090°C and fO_2 buffered at NNO, show that this basalt, chemically represented by melt inclusions in olivine $Fo_{\sim 80}$ (TAN 23-18 and 26; Table 4), cannot differentiate into Yasur-type basaltic-trachyandesite if it initially contains more than ~1 wt % of water. For 2 wt % H_2O, as measured in the TAN 23-18 inclusion, both isobaric crystal fractionation at 300 MPa and polybaric melt differentiation from 300 to 200 MPa fail to reproduce the Yasur magma composition and mineral paragenesis. At 1100–1090°C, the basalt would crystallize for only 20%, with clinopyroxene being prevalent, whereas plagioclase starts crystallizing at low temperature (≤1090°C). As a result, Al_2O_3 drastically increases (up to 19 wt %) whereas CaO decreases in the melt, which is opposite to what is observed in the natural samples (Tables 1 and 2). For a higher initial H_2O amount, the basalt crystallization rate is lower or even negligible. These conclusions remain valid under redox conditions more oxidizing than NNO. Instead, with 0·8–1 wt % of dissolved H_2O the basalt is able to crystallize extensively (45–30%), forming plagioclase (An_{71-68}), olivine (Fo_{75-71}), clinopyroxene, and a little spinel in the 1110–1080°C range, which does correspond to the paragenesis of the poorly crystallized Yasur basaltic-trachyandesite (sample TAN 6). Therefore, the basalt feeding the Yasur–Siwi system must be weakly hydrous to differentiate into basaltic-trachyandesite. Depending on its actual dissolved CO_2 content, we infer that this basalt could be emplaced between about 11 km and ~6 km depth beneath the Siwi caldera, before differentiating into basaltic-trachyandesite.

Yasur–Siwi basaltic-trachyandesites

Our dataset for dissolved CO_2 and H_2O in olivine-hosted melt inclusions and glass embayments in the Yasur basaltic-trachyandesite is much larger. It indicates polybaric melt entrapment in olivine at total ($P_{CO2} + P_{H2O}$) pressures ranging from about 130 MPa to <50 MPa (Fig. 11; Electronic Appendix 3). A similar pressure range, from ~110 to <50 MPa, is inferred for the few analogous inclusions from the Siwi sequence (TAN 1 and 17; Electronic Appendix 3). We thus infer that basaltic-trachyandesite, having on average 10% crystals and ~1·0–1·3 wt % of dissolved H_2O, is emplaced and degasses at between ~4–5 km and <~1·8 km depth beneath Siwi caldera. This magma is directly erupted only during the vigorous explosive activity, which produces the distal fallout deposits. Otherwise, during 'standard' Yasur explosive activity the magma experiences an additional late stage of degassing and crystallization, probably at shallow depth, as demonstrated by the high crystal (32%) and low bulk H_2O contents (0·2–0·3 wt %) of the proximal scoriae. MELTS calculations do reproduce the crystallization extent and mineral paragenesis of these water-poor ejecta, within a temperature range of 1090–1100°C, under NNO redox conditions and a total pressure of <50 to 10 MPa (<1·8 to 0·37 km depth). Plagioclase (An_{56-53}) is the prevalent phenocryst phase (~27–30%), coexisting with ~1–1·5% olivine (Fo_{70}), 1·6–2%, spinel, and a negligible fraction of clinopyroxene, as actually observed in these scoriae. Under more oxidizing conditions (NNO > +0·5), we find that the olivine either disappears or is significantly richer in MgO (Fo ~74) than measured in our representative TAN 12 sample.

In summary, distal and proximal scoriae from Yasur share comparable bulk-rock compositions and crystallization temperatures, but differ in their crystal and volatile contents, and in their glassy matrix compositions. These samples provide a clear illustration of the prevalent role of water exsolution, at nearly constant temperature, in promoting shallow crystallization. Crystal-rich degassed magma, expelled as bombs and vesicular scoriae during typical Strombolian (or Vulcanian) activity, is actually stored at shallow depths in the upper Yasur volcanic conduits.

We also outline that the relatively high crystallization temperature of the basaltic-trachyandesites, irrespective of their mineral paragenesis and crystal amount, requires a

Downloaded from http://petrology.oxfordjournals.org/ by guest on March 22, 2015

steady and relatively high heat flow. Basalt crystallization supplies a heat flow $\Phi H = (C_p \Delta T + \varphi L)$, where C_p is the melt heat capacity (1300–1484 J kg^{-1} K^{-1}; Bohrson & Spera, 2001), ΔT the temperature decrease, φ the fraction of crystals, and L the latent heat of crystallization [(3·5–4·2) × 10^5 J kg^{-1}; Bohrson & Spera, 2001]. A ΔT of ~55°C is assessed from the difference between the basalt liquidus temperature, calculated from MELTS (1158–1164°C for 1 wt % dissolved H_2O), and the measured temperature of basaltic-trachyandesite crystallization. We obtain a crystallization-related heat release of ~2·3 × 10^5 W kg^{-1} basalt, which could contribute to maintain the relatively elevated temperature of the overlying H_2O-poor basaltic-trachyandesites.

Magma degassing processes and budget

Magma degassing processes

Our melt inclusion dataset allows us to characterize the degassing behavior of the main volatile species (CO_2, H_2O, S and Cl) during magma differentiation and decompression in the above estimated pressure ranges beneath Siwi caldera.

As shown by Fig. 11, during decompression of the basaltic-trachyandesite magma from about 130–110 MPa to <50 MPa carbon dioxide sharply degasses, whereas H_2O does not vary much from its initial value of ~1–1·3 wt % until very shallow depths. Such a pattern strongly suggests open-system degassing conditions (e.g. Newman *et al.*, 2000). It would imply a CO_2-dominated (60–80 mol %) gas phase, whereas gas emissions are water-dominated. Moreover, if the basaltic-trachyandesite actually derives from ~50% crystal fractionation of a basalt containing ~0·8–1 wt % H_2O, it should be as twice as rich in water.

The trend depicted in Fig. 11 cannot be an artefact of mixing, in constant proportions, between the basaltic-trachyandesite and an H_2O-poor component (such as recycled degassed magma or, possibly, a residual melt of Siwi ignimbrite). Indeed, a water-poor degassed component should also be depleted in sulfur and partly in chlorine and, while mixing, would affect the distribution of these two species. This possibility is discounted by the variation of S and Cl in the olivine-hosted melt inclusions, which clearly delineates true degassing trends (Fig. 12). As also mentioned above, we have found no textural or mineralogical evidence of mixing between the low-H_2O feeding basalt and an H_2O-enriched trachyandesite.

Furthermore, several observations exclude significant H_2O re-equilibration of the analyzed melt inclusions with the carrier magma (e.g. Danyushevsky *et al.*, 2002). This process, driven by proton diffusion, can occur on short time scales but is limited during rapid ascent of magma from shallow depths (Johnson *et al.*, 2010). This is typically the case for the Yasur scoriaceous products, which experienced high cooling rates: their matrices are perfectly glassy, the morphology of both their olivine crystals and melt inclusions points to crystal nucleation induced by fast decompression events, and, most importantly, their opened glassy embayments in olivine have the same H_2O content as the sealed inclusions. All these features demonstrate limited water diffusion during magma ascent and emplacement. Accordingly, the H_2O concentrations of 1–1·3 wt % measured in the olivine-hosted melt inclusions in the Yasur distal scoria lapilli are considered representative for the basaltic-trachyandesite prior to its crystallization and eruption.

Therefore, the lower than expected H_2O content in the basaltic-trachyandesite would imply water loss either through the conduit walls or via its fluxing by deep CO_2-rich gas bubbles derived from the underlying and differentiating parental basalt. This process was recently advocated to explain magma dehydration in both basaltic (e.g. Spilliaert *et al.*, 2006; Johnson *et al.*, 2008; Collins *et al.*, 2009) and silicic (Blundy *et al.*, 2010) systems. Moreover, recent experiments involving re-equilibration of H_2O-bearing rhyolitic melts with a CO_2-rich gas phase show that fluxing by even a small quantity of CO_2 may provoke temporal volatile under-saturation of the melt and the release of large proportions of H_2O (Yoshimura & Nakamura, 2010). Although further data are needed to confirm this interpretation, it remains likely that H_2O exsolution and loss (possibly ~1 wt %) exerts the dominant control upon the genesis and crystallization path of the basaltic-trachyandesitic magma beneath Siwi caldera. In that context, we infer that the gas phase flowing through this magma will be H_2O-dominated (up to ~90 mol %), instead of CO_2-dominated, as actually observed in the surface emissions.

Focusing on the variations in H_2O, S and Cl during magma differentiation and decompression, which are the best documented, we identify a multi-stage degassing process during which these three species behave differently (Table 6). Magma differentiation is tracked by K_2O, the fraction of residual melt (f) being given by the K_2O_0/K_2O ratio (where K_2O_0 is the concentration of the melt inclusions representative of the parental basalt). During the first degassing stage, while the basalt evolves by crystal fractionation towards the basaltic-trachyandesite ($f = 0·46$), ~40% of the total H_2O and 63% of the total sulfur become exsolved and lost (Fig. 12a, Stage I in Table 6). In contrast, Cl loss is negligible as the Cl/K_2O (0·046) remains unchanged (Fig. 12b). Chlorine exolution is recorded by the large sealed melt inclusions in the Yasur distal scoriae (Stage II in Table 6), and by the basaltic-trachyandesitic melts (TAN 1 and 17) from the Siwi ignimbrite sequence (Fig. 12). During this stage of concomitant Cl and S degassing, crystallization is almost negligible. Finally, the ultimate degassing stage (Stage III in Table 6) is represented by the evolved ($f = 0·35$)

Downloaded from http://petrology.oxfordjournals.org/ by guest on March 22, 2015

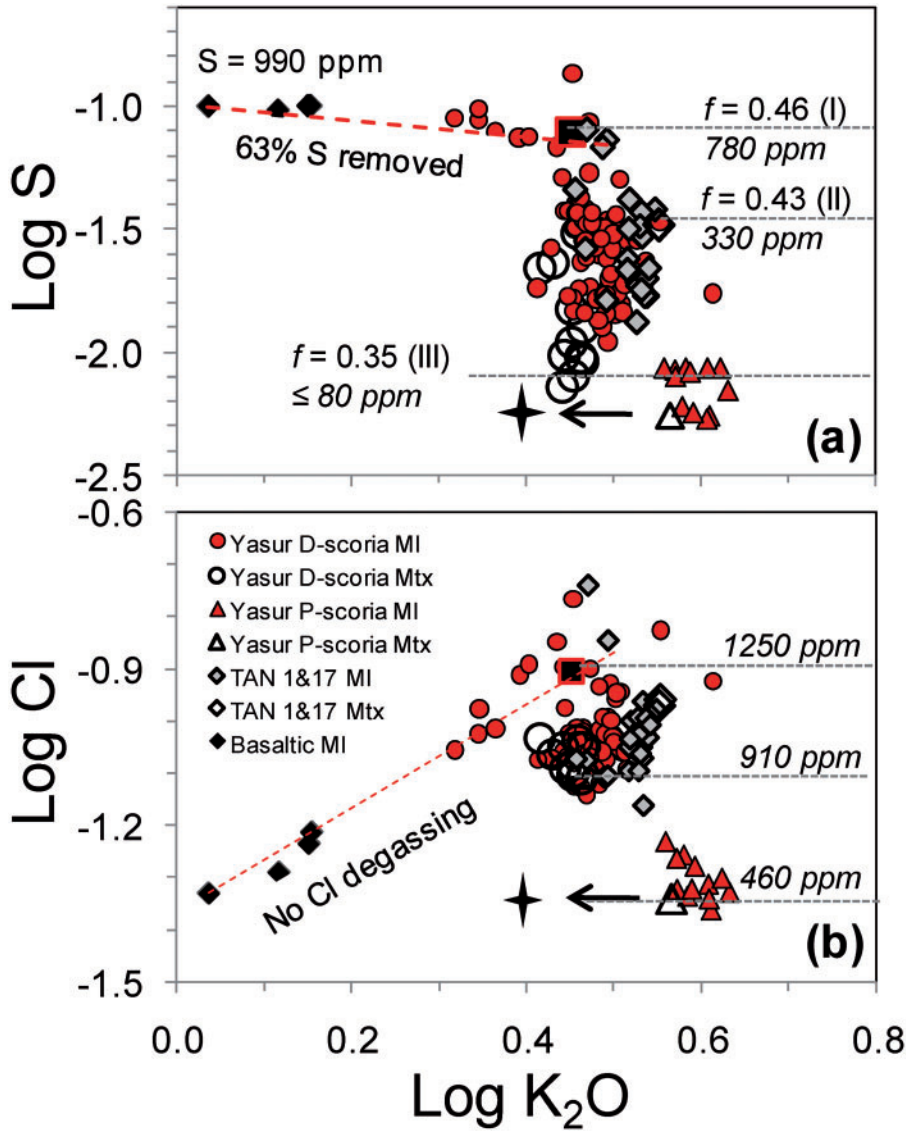

Fig. 12. Log–log diagrams of S (a) and Cl (b) evolution vs K_2O in Yasur and Siwi melt inclusions and glassy matrices. *f*, extent of melt evolution derived from the K_2O/K_2O_0 ratio. Sulfur is exsolved during a first stage (Stage I) of basalt differentiation, whereas Cl purely tracks the degassing of the basaltic trachyandesite (Stages II and III). The star represents the bulk volatile content of shallow crystal-rich basaltic-trachyandesite, corrected for the amount of crystals (32%), which demonstrates their marked depletion in Cl. Excluding these latter samples, the variation of the melt inclusion S and Cl contents in samples TAN 1 and TAN 17 (Siwi sequence) overlaps that measured in Yasur samples. D- and P-scoria refer to scoriae from distal and proximal deposits, respectively.

trachyandesitic melt inclusions and matrix glasses of the proximal ejecta, which are strongly depleted in both H_2O ($\leq$0·4 wt %) and S ($<$80 ppm) and extensively impoverished in Cl (~560–460 ppm). Taking account of their extent of crystallization (32%), these ejecta are twice as degassed in chlorine as the magma that is erupted and quenched during periods of more vigorous explosive activity. This difference cannot be ascribed to the limited variation of the [(Al + Na + Ca + Mg)/Si] mole ratio of the melt inclusions (0·35 and 0·45 in proximal and distal samples, respectively). Rather, it indicates a strong control of diffusion kinetics on late-stage Cl degassing, while gas bubbles and/or slugs are flowing across the ponding and crystallizing upper magma column, with chlorine being efficiently partitioned into the H_2O-rich vapor (Webster *et al.*, 1999).

Simple mass-balance calculations show that, during this multi-stage degassing process, the S/Cl molar ratio of the equilibrium gas phase will vary noticeably, from an average of 5·9 when magma degasses in the ~100–50 MPa

Downloaded from http://petrology.oxfordjournals.org/ by guest on March 22, 2015

Table 6: Volatile element ratios in vapor phase deduced from melt inclusion data and degassing budget

	Basalt	Yasur basaltic trachyandesite		
MI/Mtx:	MI	MI	MI	Mtx*
Host (Fo mol %):	80–77	74	74	
K_2O_0/K_2O (*f*)	1	0·46	0·43	0·35
K_2O (wt %)	1·3	2·8	3·0	3·7
H_2O (wt %)	1·0	1·2	1·2	0·2
S (wt ppm)	990	780	330	60†
Cl (wt ppm)	553	1247	910	460
F (wt ppm)	n.d.	n.d.	350	360
CO_2 (wt ppm)	573	n.d.	230–120	n.d.

	Step-by-step volatile loss			
	Stage I	Stage II	Stage III	Total budget
K_2O_0/K_2O (*f*)	0·46	0·43	0·35	
ΔH_2O (wt %)	0·45	0·5	1·1	0·94
H_2O loss fraction	0·45	0·5	0·9	0·94
ΔS (wt ppm)	628	847	735	969
S loss fraction	0·63	0·86	0·9	0·98
ΔCl (wt ppm)	0	159	899	391
Cl loss fraction	0 or negligible	0·29	0·72	0·71
Calculated molar ratios in vapor phase				
S/Cl	∞	5·9	0·9	2·7
H_2O/SO_2	13	10	26	17

Stage I: degassing recorded by MI, without Cl loss, in Yasur distal scoriae (*f* from 1 to 0·46). Stage II: degassing recorded by large sealed inclusion in distal scoriae (*f* from 1 to 0·43). Stage III: shallow degassing of the Yasur magma (*f* from 0·46 to 0·35).
*Glassy matrix of proximal vesicular scoriae.
†Lower than the detection limit (80 ppm).

Table 7: Volumes of degassing magmas

SO_2 flux (tons d^{-1})	680
ΔS (wt ppm)	969
Mass of degassed basaltic magma (kg s^{-1})	$4{\cdot}1 \times 10^3$
Volume of degassed basaltic magma (m^3 a^{-1})	$4{\cdot}9 \times 10^7$
HCl flux (tons d^{-1})*	165
ΔCl (ppm)	899
Mass of degassed basaltic-trachyandesite (kg s^{-1})	$2{\cdot}1 \times 10^3$
Volume of degassed basaltic-trachyandesite (m^3 a^{-1})†	$2{\cdot}6 \times 10^7$
Cumulative YRB uplift (m^3 a^{-1})	$2{\cdot}8 \times 10^6$
Vol. degassed magma/vol. YRB	9

*HCl flux (tons d^{-1}) normalized to the time-averaged SO_2 flux of 680 tons d^{-1}.
†Of the degassed basaltic-trachyandesite magma 95% is accumulated beneath the Yenkahe horst.

pressure interval to ~1·0 during the final (shallow) degassing stage. Therefore, deeply derived gas slugs driving the recurrent Yasur explosions should display high S/Cl ratios, as actually observed (Oppenheimer *et al.*, 2006; Allard *et al.*, in preparation), whereas purely residual degassing of the upper magma column should be characterized by a low (≤1) S/Cl ratio. The time-averaged S/Cl ratio of 2·4 we measured for both passive and explosive crater gas emissions in October 2007 thus requires a mixed contribution of shallow (≤1) and deeper-derived (≥5·9) magmatic gas. It should be noted that the steady S/Cl ratio of ~2·0 for purely passive emissions, as measured in January 2005 (Oppenheimer *et al.*, 2006), also requires a two-component gas mixture, but with enhanced contribution of the shallow gas phase. These observations further support a differential gas transfer (i.e. open-system degassing) across the magma plumbing system, as already suggested by the CO_2–H_2O degassing pattern in Fig. 11.

Magma degassing budget

As a whole, we compute a bulk loss of ≥94% for H_2O and S, and of 70% for Cl during magma degassing beneath Siwi caldera (Table 6). Combined with the Yasur gas fluxes, the degassed mass fraction of each volatile species allows us to quantify the amounts of degassing magma that sustain the current eruptive activity (Table 7). From the pre-eruptive S content of the basalt and the time-averaged SO_2 flux of 680 tons d^{-1} representative for the last 5 years of activity (Bani & Lardy, 2007), we infer a bulk magma degassing rate of $4{\cdot}1 \times 10^3$ kg s^{-1}, or $\sim 5 \times 10^7$ m^3 a^{-1}, for a mean density of 2650 kg m^{-3}. Chlorine, which does not exsolve during basalt differentiation, purely tracks degassing of the basaltic-trachyandesite between about 5 and 4 km depth and the surface. From its bulk loss (Table 6) and the mean HCl emission rate (165 tons d^{-1}), we derive a degassing rate of $2{\cdot}1 \times 10^3$ kg s^{-1}, or $2{\cdot}6 \times 10^7$ m^3 a^{-1}, of basaltic-trachyandesite. Hence, the degassing of nearly equivalent amounts of basalt and basaltic-trachyandesite sustains the overall volcanic gas output. Considering the uncertainties involved in these calculations, we find a good agreement between the proportion inferred from volatile species and the rate (~50%) of basalt fractionation needed to generate the basaltic-trachyandesite constrained from the major and trace element data. This implies that, even though the analyzed basalt is not a true primitive magma, one should

Downloaded from http://petrology.oxfordjournals.org/ by guest on March 22, 2015

not significantly underestimate its pre-eruptive sulfur content and, hence, the computed bulk magma degassing rate.

Because about 60% of the total sulfur and thus of the SO_2 flux from Yasur derive from basalt degassing, a differential flow of S-bearing gas bubbles must occur through the overlying basaltic-trachyandesite. This same conclusion applies to deeper exsolved CO_2 but also to H_2O, 1 wt % of which may be exsolved during basalt differentiation. A differential transfer of gas bubbles nucleated in the basalt and already enriched in CO_2, H_2O and SO_2 is indeed consistent with the open-type degassing process suggested by the P-related CO_2–H_2O concentrations in the Yasur products (Fig. 11). We note here that the H_2O/SO_2 molar ratio inferred for bulk degassing of the basalt (~17; Table 6) is much lower than the mean H_2O/SO_2 ratio (70; range 50–90) measured in Yasur gas emissions. However, we have seen that the latter are affected by a large uncertainty, owing to correction for ambient air background. Moreover, we do not know whether the emitted water vapor is wholly magmatic in origin or may partly derive from entrainment of external steam of meteoric or/and hydrothermal origin into the shallow plumbing system of Yasur. This latter possibility is compatible with the observation of magma–water interactions in the Yasur volcanic deposits, with the presence of a widespread hydrothermal system beneath the Yenkahe horst (Gauthier *et al.*, 2001*l*, in preparation), and with the heavy local rainfall recharge and highly permeable nature of the Yasur volcanic cone.

Relationship between magma supply and the Yenkahe block resurgence

Coral reef terraces on the Yenkahe resurgent block record a sequence of uplifts with two sharp events dated at AD 1002 and 1878 (Chen *et al.*, 1995). The 10–15 m uplift that occurred in 1878 was consecutive with a local earthquake, not felt 20 km away, and was not registered by coral reefs standing a few hundred meters from the uplifted area, as noted by Chen *et al.* (1995). Those workers thus concluded that the Yenkahe resurgence was strictly confined within the Siwi caldera and was probably due to magma emplacement or movement at shallow depth. From the geometry of the Yenkahe resurgent block and its average uplift of $15{\cdot}6\,cm\,a^{-1}$ during the last millenium (Chen *et al.*, 1995), we compute a cumulative volume uplift of $2{\cdot}8 \times 10^6\,m^3\,a^{-1}$, or $2{\cdot}8\,km^3$ in 1000 years.

It is of interest to compare this cumulative deformation with the magma degassing rates during the same interval. To maintain the steady eruptive activity of Yasur and the great homogeneity of its products for 1000 years at least, the magma degassing rates must correspond to supply rates, and present-day average values can reasonably be extrapolated to the past. A bulk influx of $\sim 5 \times 10^7\,m^3\,a^{-1}$ of basaltic magma, as deduced from the time-averaged SO_2 flux and the S content of basaltic melt inclusions, would correspond to a cumulative basaltic supply of $\sim 50\,km^3$ in 1000 years. Our data for chlorine degassing show that about a half ($\sim 26\,km^3$) of this supply should have differentiated into the basaltic-trachyandesite that has sustained the Yasur eruptive activity. The proportion of this latter magma extruded in 1000 years is not easy to assess, but can be roughly estimated from the volumes of the Yasur volcanic cone and Yasur-related tephra deposits. The Yasur cone, made of ash, coarse lapilli, bombs and lava, has a base diameter of 1·5 km and a height of 210 m, which, given its morphology, implies a volume of $<0{\cdot}2\,km^3$. The Yasur deposits derive from the standard eruptive activity plus occasional more powerful events, about one every 20–30 years, whose explosivity index (VEI) is at most three (Carney & MacFarlane, 1979). For these stronger explosive events, we estimate a maximum production of 0·3–0·4 km^3 of dense magma. For the standard activity, we use the emission rate of volcanic ash produced by Yasur explosions and transported downwind of the crater, estimated as $5 \times 10^5\,kg\,d^{-1}$ from filter-pack sampling of the particulate matter in October 2007 and the SO_2 plume flux (Allard *et al.*, in preparation). For an ash particle density of between 1500 and 2000 $kg\,m^{-3}$, the corresponding volume of dense erupted magma approximates $\sim 0{\cdot}4$–$0{\cdot}6\,km^3$ in 1000 years. The lava bomb production, roughly estimated as $200\,m^3\,d^{-1}$ (Gauthier *et al.*, 2001*l*), would correspond to a minor dense output of $0{\cdot}05\,km^3$ in 1000 years, taking account of the high vesicularity of most of these ejecta. As a whole, therefore, only about $1\,km^3$ of magma may have been erupted from Yasur in that time interval, which means that 95% ($\sim 25\,km^3$) of the supplied (degassed) basaltic-trachyandesite should have accumulated beneath the Siwi caldera complex. Such a high proportion of unerupted to erupted magma is typical for open-conduit basaltic volcanoes, such as Stromboli (Allard *et al.*, 2008).

We thus find that, in 1000 years, the volume of degassed basaltic-trachyandesite accumulated beneath the Siwi caldera is about 10 times larger than the cumulative deformation of the Yenkahe block and, therefore, could easily account for its resurgence. The storage of $\sim 25\,km^3$ of degassed and hence dense molten magma beneath the 5·5 km long by 3 km wide Yenkahe horst could have formed an accreting sill-like body of 1·5 km height, crystallizing on its margins and conductively heating the host rocks and the overlying hydrothermal system. The low magmatic CO_2 content of local thermal waters (Gauthier *et al.*, 2001*l*, in preparation) and soil gas emanations (Chaput *et al.*, 2009; P. Allard *et al.*, unpublished data, 2007), attributed to the extensive hydrothermal alteration and sealing of volcanic rocks forming the Yenkahe block (Chaput *et al.*, 2009), would also be consistent with relatively shallow emplacement of the roof of this degassed magma body. The intrusive body, with almost zero eruptive potential, must be connected to the deeper feeding

Downloaded from http://petrology.oxfordjournals.org/ by guest on March 22, 2015

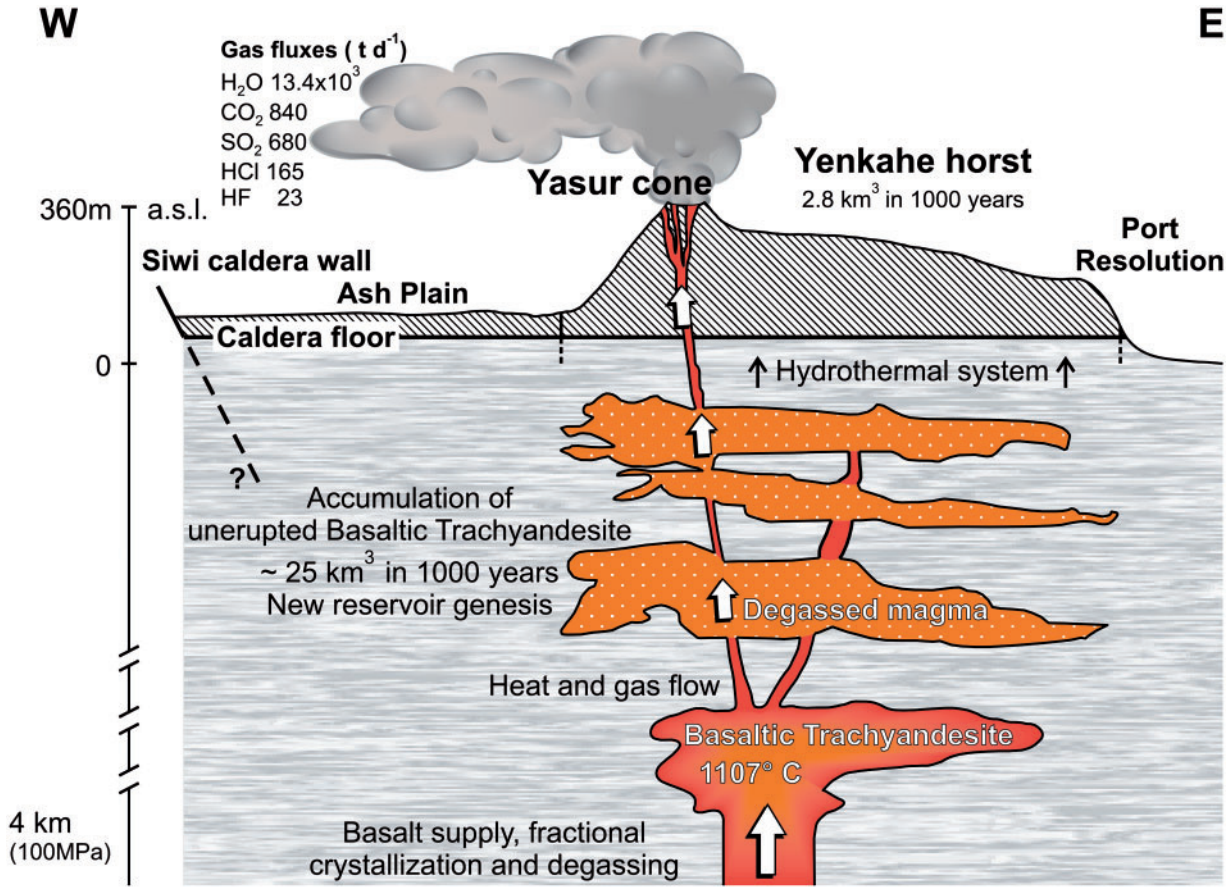

Fig. 13. Schematic representation, not to scale, of the magmatic plumbing system beneath Siwi caldera. Both gas and melt inclusion data lead us to propose that ~25 km^3 of degassed basaltic-trachyandesite may have accumulated beneath the Yasur–Siwi volcanic complex during the last 1000 years, which is one order of magnitude larger than the accumulated deformation of the Yenkahe resurgent block over the same time interval. (Note that these relative proportions are not respected in our illustration.)

system by some dyke-like pathways that allow gas bubbles and batches of the undegassed basaltic-trachyandesite to rise and sustain the Yasur eruptive activity. The Yasur vent can thus be viewed as a pipe linked to the accreting magma body, through which most of the gas supplied to the system escapes separately (Fig. 13). GPS measurements made in 2002–2005 have revealed short-term episodes of horizontal deformation and rapid inflation then deflation of the Yenkahe horst, reaching an amplitude of 17 cm over a few months and associated with a temporary increase then a decrease in Yasur activity (Erre, 2005). Such rapid and reversed deformations strongly suggest transient pressuring of the magma body owing to an enhanced influx of magmatic gases, rather than a magma intrusion. Temporal variations in magmatic gas influx from either the underplating basalt or the basaltic-trachyandesite, or both, could explain the observed oscillations in Yasur's eruptive regime (Erre, 2005) and SO_2 emission rate (Bani & Lardy, 2007). The associated episodes of rapid inflation and deflation of the Yenkahe horst detected with GPS, possibly amplified by the shallow hydrothermal system, indicate an almost elastic reponse of the medium to these short-term variations in gas supply.

In the long term, however, the accumulated uplift and extension (graben) of the Yenkahe block, with episodes of sharp co-seismic uplift, require magma accumulation with occasional brittle fracturing of the caldera floor. Rock fracturing and tensile failure in volcanic systems are known to depend on several parameters, such as the strength of the volcanic rocks, the deformation mode (elastic or viscoelastic), and the mechanical response of the magma reservoir to its pressurization (e.g. Simakin & Ghassemi, 2010). It has to be stressed that the sudden block faulting and large co-seismic uplift that affected the eastern part of the Yenkahe block in 1878 (Chen *et al.*, 1995) was not accompanied or followed by a major change in Yasur activity. Such a decoupling between violent co-seismic uplift and volcanic activity negates a sudden magma recharge as the trigger of that event. Rather, it is compatible with a sudden mechanical release of accumulated stress, facilitated by previous faulting of a weakened structure. Hence, we propose that Yenkahe block

Downloaded from http://petrology.oxfordjournals.org/ by guest on March 22, 2015

resurgence in the past millennium could result from both continuous and discontinuous (co-seismic) accommodation of the mechanical stress generated by the gradual storage of degassed basaltic-trachyandesite magma, at a mean rate of $\sim 0{\cdot}025\ km^3\ a^{-1}$, beneath the Siwi caldera. We note that a comparable magma and gas supply rate ($0{\cdot}02\ km^3\ a^{-1}$) was inferred to explain the resurgent dome inflation ($0{\cdot}04\ m\ a^{-1}$) in Long Valley caldera between 1978 and 1999 (Hill, 2006), despite the much larger dimensions of that caldera. The respective influence of magma intrusion, gas supply and hydrothermal systems on ground deformation in calderas, however, remains strongly debated. We emphasize that the Yasur–Siwi volcanic complex, with its long-term and fast deformation of the caldera floor, short-term deflation–inflation phases most probably caused by magmatic gas motion, and persistent eruptive activity, is a most suitable site to address these questions quantitatively.

CONCLUSIONS

We provide here new data on the petrology of the Yasur–Siwi volcanic products, the first results on their pre-eruptive volatile contents, and the first complete budget for Yasur gas emissions. Together, the results allow us to quantify the rates of magma and volatile supply to this volcanic complex during a post-caldera stage and to propose initially a structure of its plumbing system. We outline the following main observations and conclusions.

(1) The geochemistry of Yasur–Siwi bulk products and of their melt inclusions, together with literature data for associated basalts, strongly suggests the long-term feeding of Tanna volcanism by a homogeneous arc basaltic magma. This conclusion could be reinforced by further study of the Tanna basalts themselves.

(2) Yasur basaltic-trachyandesites derive from ~50% crystal fractionation of a parental basalt moderately enriched in volatiles, and according to their dissolved H_2O and CO_2 contents, should be emplaced between $\leq$5–4 km depth and the surface. Their constant bulk composition and mineralogy during the last 1400 years, as well as their high mean temperature ($1107 \pm 15^{\circ}C$), imply a steady regime of crystallization. Their early dehydration and prevalent open-system degassing generate a gas phase gradually richer in H_2O, S and then Cl upon decompression.

(3) Yasur magmas erupted during normal and more powerful explosive activity share a comparable bulk composition and crystallization temperature, but noticeably differ in their crystal contents, volatile abundances and glassy matrix compositions. These features indicate a prevalent role for water exsolution, at nearly constant temperature, in promoting shallow crystallization of the magma filling the upper Yasur conduits, which is represented by light scoriae and vesicular to dense bombs, rich in crystals, thrown out on the upper volcanic cone.

(4) Yasur volcano emits H_2O-rich (97 mol %) magmatic gas at an average rate of $13{\cdot}4 \times 10^3\ tons\ d^{-1}$, which makes it a typical arc emitter. The amount of feeding basaltic magma needed to sustain this gas output, computed from its initial S content and the time-averaged SO_2 flux ($680\ tons\ d^{-1}$), averages $4{\cdot}1 \times 10^3\ kg\ s^{-1}$, nearly half of which is differentiated into basaltic-trachyandesite. This implies the development of a large deep magma reservoir able to accommodate the accumulated volume of basalt over the last 1000 years. Basalt crystallization would supply a heat flow of ~1 MW to the overlying basaltic-trachyandesite, thereby contributing to maintain the relatively elevated temperature of this otherwise H_2O-poor magma.

(5) The time-averaged HCl flux of $165\ tons\ d^{-1}$ is essentially supplied by the degassing of basaltic-trachyandesite at a rate of $0{\cdot}026\ km^3\ a^{-1}$, most (>95%) of which remains unerupted. The respective amounts of degassing basalt and basaltic-trachyandesite are in good agreement with independent estimates from petrological data.

(6) Over the last 1000 years, $\sim 25\ km^3$ of basaltic-trachyandesite would have degassed without erupting and, therefore, been stored in an accreting intrusive body beneath Siwi caldera. This amount is one order of magnitude larger than the accumulated deformation of the Yenkahe resurgent block. We thus suggest that ground deformation of the caldera floor could result from both continuous and discontinuous (co-seismic) mechanical relaxation of the stress induced by this accumulation of unerupted degassed magma.

ACKNOWLEDGEMENTS

Our fieldwork greatly benefited from local support from B. Pelletier (IRD), the French Embassy in Port-Vila and Air Vanuatu. We thank D. Edouard and A. Beaumais for their involvement in data acquisition, P. Pantani for graphical assistance, D. P. Hill and A. Hirn for useful discussions, C. Erre and M. Lardy for providing us with GPS data on Yenkahe horst, and B. Scott for providing us with the New Zealand Geological Survey 1988 report. Reviews by D. Pyle, P. Ruprecht, M. Humphreys and J. Stix greatly helped in improving the paper.

FUNDING

This work was supported by ANR contracts ANR-06-CATT-02 Arc-Vanuatu and ANR-06-CATT-012 Volgaspec. Field missions of A.B. and A.A. were funded

Downloaded from http://petrology.oxfordjournals.org/ by guest on March 22, 2015

by the INGV-Pisa (Italy), and the Università di Palermo (Italy), respectively. This paper is IPGP Contribution 3133.

SUPPLEMENTARY DATA

Supplementary data for this paper are available at *Journal of Petrology* online.

REFERENCES

Acocella, V., Cifelli, F. & Funiciello, R. (2000). Analogue models of collapsed calderas and resurgent domes. *Journal of Volcanology and Geothermal Research* **104**, 81–96.

Aiuppa, A. (2009). Degassing of halogens from basaltic volcanism: Insights from volcanic gas observations. *Chemical Geology* **263**, 99–109.

Aiuppa, A., Federico, C., Giudice, G. & Gurrieri, S. (2005). Chemical mapping of a fumarolic field: La Fossa crater, Vulcano island (Aeolian islands, Italy). *Geophysical Research Letters* **32**, L13309, doi:10.1029/2005GL023207.

Aiuppa, A., Moretti, R., Federico, C., Giudice, G., Gurrieri, S., Liuzzo, M., Papale, P., Shinohara, H. & Valenza, M. (2007). Forecasting Etna eruptions by real-time observation of volcanic gas composition. *Geology* **35**, 1115–1118.

Aiuppa, A., Giudice, G., Gurrieri, S., Liuzzo, M., Burton, M., Caltabiano, T., McConigle, A. S. J., Salerno, G., Shinohara, H. & Valenza, M. (2008). Total volatile flux from Mount Etna. *Geophysical Research Letters* **35**, L24302, doi:10.1029/2008GL035871.

Allard, P., Aiuppa, A., Burton, M., Caltabiano, T., Federico, C., Salerno, G. & La Spina, A. (2008). Crater gas emissions and the magma feeding system of Stromboli volcano. In: Calvari, S., Inguaggiato, S., Puglisi, F., Ripepe, M. & Rosi, M. (eds) *Learning from Stromboli. Geophysical Monograph, American Geophysical Union* **182**, 65–80.

Allard, P., Aiuppa, A., Bani, P., Métrich, N., Bertagnini, A., Gauthier, P.-J., Parello, F., Sawyer, G., Shinohara, H., Bagnato, E., Mariet, C. & Garaebiti, E. (2009). Ambrym basaltic volcano (Vanuatu Arc). Volatile fluxes, magma degassing rate and chamber depth. *EOS Transactions, American Geophysical Union* **90**, 52, Abstract V24C-04.

Allen, S. R. (2005). Complex spatter- and pumice-rich pyroclastic deposits from an andesitic caldera forming eruption: The Siwi pyroclastic sequence, Tanna, Vanuatu. *Bulletin of Volcanology* **67**, 27–41.

Andres, R. J. & Kasgnoc, A. D. (1998). A time averaged inventory of subaerial volcanic sulfur emissions. *Journal of Geophysical Research* **103**, 25251–25261.

Arthur, M.A. (2000). Volcanic contributions to the carbon and sulfur geochemical cycles and change. In: Sigurdsson, H. (ed.) *Encyclopedia of Volcanoes*. San Diego, CA: Academic Press, pp. 1045–1056.

Aubert de la Rüe, E. (1960). Les manifestations actuelles du volcanisme aux Nouvelles Hébrides (Mélanésie). *Bulletin Volcanologique* **23**, 197–205.

Bani, P. & Lardy, M. (2007). Sulphur dioxide emission rates from Yasur volcano, Vanuatu archipelago. *Geophysical Research Letters* **34**, L20309, doi:10.1029/2007GL030111.

Bani, P., Oppenheimer, C., Tsanev, V.I., Carn, S.A., Cronin, S.J., Crimp, R., Calkins, J.A., Charley, D., Lardy, M. & Roberts, T.R. (2009). Surge in sulphur and halogen degassing from Ambrym volcano, Vanuatu. *Bulletin of Volcanology* **71**, 1159–1168, doi:10.1007/s00445-009-0293-7.

Blundy, J., Cashman, K., Rust, A. & Witham, F. (2010). A case for CO_2-rich arc magmas. *Earth and Planetary Science Letters* **290**, 289–301.

Bohrson, W. A. & Spera, F. J. (2001). Energy-constrained open-system magmatic processes II. Application of energy-constrained assimilation–fractional crystallization (EC-AFC) model to magmatic systems. *Journal of Petrology* **42**, 1019–1042.

Burton, M. R., Allard, P., Muré, F. & La Spina, A. (2007). Magmatic gas composition reveals the source depth of slug-driven Strombolian explosive activity. *Science* **37**, 227–230.

Calmant, S., Pelletier, B., Lebellegard, P., Bevis, M., Taylor, F. W. & Phillips, D. A. (2003). New insights on the tectonics along the New Hebrides subduction zone based on GPS results. *Journal of Geophysical Research* **108**(B6): 2319–2339.

Carignan, J., Hild, P., Mevelle, G., Morel., J. & Yeghicheyan, D. (2001). Routine analyses of trace elements in geological samples using flow injection and low pressure on-line liquid chromatography coupled to ICP-MS: A study of geochemical reference materials BR, DR-N, UB-N, AN-G and GH. *Geostandards Newsletter* **25**, 187–198.

Carnay, J. N. & MacFarlane, A. (1979). *Geology of Tanna, Aneityum, Futuna and Aniva. New Hebrides Geological Survey Report* 5–29.

Chaput, M., Dumont, S., Lenat, J. F., Finizola, A., Gaillet, L., Barde Cabusson, S., Byrdina, S., Menny, P., Peltier, A., Colonge, J., Douillet, G., Letort, G., Bachèlery, P., Nakedau, P. & Garaebiti, E. (2009). Structure and hydrothermal system of Yasur volcano (Vanuatu archipelago) inferred from gravimetry, electric resistivity tomography, time domain electro-magnetism, self-potential, subsurface temperature and soil CO_2 concentration, SOPAC 38th Session, 21–29 October 2009, Port Vila, Vanuatu, SOPAC Miscellaneaous report 700, Abstract.

Chen, J. K., Taylor, F. W., Edwards, R. L., Cheng, H. & Burr, G. S. (1995). Recent emerged reef terraces of the Yenkahe resurgent block, Tanna, Vanuatu: implications for volcanic, landslide and tsunami hazards. *Journal of Geology* **103**, 577–590.

Collins, S. J., Pyle, D. M. & Maclennan, J. (2009). Melt inclusions track pre-eruption storage and dehydration of magmas at Etna. *Geology* **37**, 571–574, doi:10.1130/G30040A.1.

Danyushevsky, L. V., McNeill, A. W. & Sobolev, A. V. (2002). Experimental and petrological studies of melt inclusions in phenocrysts from mantle-derived magmas: an overview of techniques, advantages and complications. *Chemical Geology* **183**, 5–24.

Dvorak, J. & Dzurizin, D. (1997). Volcano geodesy: the search of magma reservoirs and the formation of eruptive vents. *Reviews in Geophysics* **35**, 343–384.

Elliott, T. (2003). Tracers of the slab. In: Eiler, J. (ed.) *Inside the Subduction Factory. Geophysical Monograph, American Geophysical Union* **138**, 23–43.

Erre, C. (2005). GPS characterization of vertical movements at Yasur and Lopevi active volcanoes in Vanuatu arc. Real-time RTK-GPS measurements, INSA report, Strasbourg, 210 pp. (in French) http://www.insa-strasbourg.fr/fr/gilbert-ferhat/index.html.

Faure, F. & Schiano, P. (2005). Experimental investigation of equilibration conditions during forsterite growth and melt inclusion formation. *Earth and Planetary Science Letters* **236**, 882–898.

Freda, C., Baker, D. R. & Scarlato, P. (2005). Sulfur diffusion in basaltic melts. *Geochimica et Cosmochimica Acta* **69**, 5061–5069.

Galle, B., Oppenheimer, C., Geyer, A., McGonigle, A. J. S., Edmonds, M. & Horrocks, L. (2003). A miniaturised ultraviolet spectrometer for remote sensing of SO_2 fluxes; a new tool for volcano surveillance. *Journal of Volcanology and Geothermal Research* **119**, 241–254.

Downloaded from http://petrology.oxfordjournals.org/ by guest on March 22, 2015

Gauthier, P.-J., Goff, F., Love, S. & Counce, D. (2001). Geochemical surveillance of fluid and gas discharges at Yasur volcanic complex, Tanna island, Vanuatu. *EUG XI General Assembly, Strasbourg, France*, Abstract H6.2024.

Ghiorso, M. S. & Sack, R. O. (1995). Chemical transfer in magmatic processes IV. A revised and internally consistent thermodynamic model for the interpolation and extrapolation of liquid–solid equilibria in magmatic system at elevated temperatures and pressures. *Contributions to Mineralogy and Petrology* **119**, 197–212.

Gillot, P. Y., Chiesa, S., Pasquaré, G. & Vezzoli, L. (1982). <33,000-yr K–Ar daring of the volcano-tectonic horst of the isle of Ischia, Gulf of Naples. *Nature* **299**, 242–245.

Hill, D. P. (2006). Unrest in Long Valley caldera, California, 1978–2004. In: Troise, C., De Natale, G. & Kilburn, C. R. J. (eds) *Mechanisms of Activity and Unrest at Large Calderas. Geological Society, London, Special Publications* **269**, 1–24.

Hill, D. P., Bailey, R. A. & Ryall, A. S. (1985). Active tectonic and magmatic processes beneath Long Valley Caldera, Eastern California: An overview. *Journal of Geophysical Research* **90**(13): 11111–11120.

Hofmann, A. W. (1988). Chemical differentiation of the Earth: the relationship between mantle, continental crust, and oceanic crust. *Earth and Planetary Science Letters* **90**, 297–314.

Johnson, M. C. & Plank, T. (1999). Dehydration and melting experiments constrain the fate of sediments. *Geochemistry, Geophysics, Geosystems* **1**, 1999GC000014.

Johnson, E. R., Wallace, P. J., Cashman, K., Delgado-Granados, V. & Kent, A. (2008). Magmatic volatile contents and degassing-induced crystallization at Volcan Jorullo, Mexico: Implications for melt evolution and the plumbing systems of monogenetic volcanoes. *Earth and Planetary Science Letters* **269**, 477–486.

Johnson, E. R., Wallace, P. J., Cashman, K. V. & Granados, H. D. (2011). Degassing of volatiles (H_2O, CO_2, S, Cl) during ascent, crystallization, and eruption at mafic monogenetic volcanoes in central Mexico. *Journal of Volcanology and Geothermal Research* (in press) doi:10.1016/j.jvolgeores.2010.02.017.

Marsh, B. D. (1984). On mechanics of caldera resurgence. *Journal of Geophysical Research* **98**, 8245–8251.

Massare, D., Métrich, N. & Clocchiatti, R. (2002). High-temperature experiments on silicate melt inclusions in olivine at one atmosphere. Inference on temperatures of homogenization and H_2O concentrations. *Chemical Geology* **183**, 87–98.

Mercier, M., Di Muro, A., Giordano, D., Métrich, N., Lesne, P., Pichavant, M., Scaillet, B., Clocchiatti, R. & Montagnac, G. (2009). Influence of glass polymerisation and oxidation on microRaman water analysis in alumino-silicate glasses. *Geochimica et Cosmochimica Acta* **73**, 197–217, doi:10.1016/j.gca.2008.09.030.

Mercier, M., Di Muro, A., Métrich, N., Giordano, D., Belhadj, O. & Mandeville, C. W. (2010). Spectroscopic analysis (FTIR, RAMAN) of water in mafic and intermediate glasses and glass inclusions. *Geochimica et Cosmochimica Acta* **74**, 5641–5656, doi:10.1016/j.gca.2010.06.020.

Métrich, N. & Wallace, P. (2008). Volatile abundances in basaltic magmas and their degassing paths tracked by melt inclusions. In: Putirka, K. & Tepley, F. (eds) *Minerals, Inclusions and Volcanic Processes. Mineralogical Society of America and Geochemical Society, Reviews in Mineralogy and Geochemistry* **69**, 363–402.

Molin, P., Acocella, V. & Funiciello, R. (2003). Structural, seismic and hydrothermal features at the border of an active intermittent resurgent block: Ischia Island (Italy). *Journal of Volcanology and Geothermal Research* **121**, 65–81.

Monzier, M., Robin, C., Eissen, J.-Ph. & Cotton, J. (1997). Geochemistry vs seismo-tectonics along the volcanic New Hebrides central Chain (Southwest Pacific). *Journal of Volcanology and Geothermal Research* **78**, 1–29.

Nabyl, A., Dorel, J. & Lardy, M. (1997). A comparative study of low frequency seismic signals recorded at Stromboli volcano, Italy and at Yasur volcano, Vanuatu. *New Zealand Journal of Geology and Geophysics* **40**, 549–558.

Nairn, I. A., Scott, B. J. & Giggenbach, W. F. (1988). Yasur volcanic investigations, Vanuatu September 1988. *New Zealand Geological Survey Report* 1–74.

Neef, G., Zhao, J. X., Collerson, K. D. & Zhang, F. S. (2003). Late Quaternary uplift and subsidence of the west coast of Tanna, south Vanuatu, southwest Pacific: U–Th ages from the raised coral reefs in the median sedimentary basin. *Australian Journal of Earth Sciences* **50**, 39–48.

Newman, S., Stolper, E. M. & Stern, R. J. (2000). H_2O and CO_2 in magmas from Mariana arc and back arc systems. *Geochemistry, Geophysics, Geosystem* **1**, 1013, doi:10.1029/1999GC000027.

Oppenheimer, C., Bani, P., Calkins, J. A., Burton, M. R. & Sawyer, G. M. (2006). Rapid FTIR sensing of volcanic gases released by Strombolian explosions at Yasur volcano, Vanuatu. *Applied Physics C* , doi:10.1007/s00340-006-2353-4.

Papale, P., Moretti, R. & Barbato, D. (2006). The compositional dependence of the saturation surface of $H_2O + CO_2$ fluids in silicate melts. *Chemical Geology* **229**, 78–95.

Peate, D. W., Pearce, J. A., Hawkesworth, C. J., Colley, H., Edwards, C. M. & Hirose, K. (1997). Geochemical variations in Vanuatu arc lavas: the role of subducted material and a variable mantle wedge composition. *Journal of Petrology* **38**, 1331–1358.

Pelletier, B., Calmant, S. & Pillet, R. (1998). Current tectonic of the Tonga–New Hebrides region. *Earth and Planetary Science Letters* **164**, 263–276.

Pyle, D. M. & Mather, T. A. (2009). Halogens in igneous processes and their fluxes to the atmosphere and oceans from volcanic activity: a review. *Chemical Geology* **263**, 110–121, doi:10.1016/j.chemgeo.2008.11.013.

Robin, C., Eissen, J.-Ph. & Monzier, M. (1994). Ignimbrites of basaltic andesite and andesite compositions from Tanna, New Hebrides arc. *Bulletin of Volcanology* **56**, 10–22.

Shinohara, H. (2005). A new technique to estimate volcanic gas composition: plume measurements with a portable multi-sensor system. *Journal of Volcanology and Geothermal Research* **143**, 319–333.

Shinohara, H., Aiuppa, A., Giudice, G., Gurrieri, S. & Liuzzo, M. (2008). Variation of H_2O/CO_2 and CO_2/SO_2 ratios of volcanic gases discharged by continuous degassing of Mt. Etna volcano, Italy. *Journal of Geophysical Research* **113**, B09203, doi:10.1029/2007JB005185.

Shinohara, H., Matsushima, N., Kazahaya, K. & Ohwada, M. (2011). Magma–hydrothermal system interaction inferred from volcanic gas measurements obtained during 2003–2008 at Meakandake volcano, Hokkaido, Japan. *Bulletin of Volcanology* (in press).

Simakin, A. G. & Ghassemi, A. (2010). The role of magma chamber–fault interaction in caldera forming eruptions. *Bulletin of Volcanology* **72**, 85–101.

Skora, S. & Blundy, J. (2010). High-pressure hydrous phase relations of radiolarian clay and implications for involvement of subducted sediment in arc magmatism. *Journal of Petrology* **51**, 2211–2243, doi:10.1093/petrology/egq054.

Spilliaert, N., Allard, P., Métrich, N. & Sobolev, A. (2006). Melt inclusion record of the conditions of ascent, degassing and extrusion of volatile-rich alkali basalt during the powerful 2002 flank eruption of Mount Etna (Italy). *Journal of Geophysical Research* **111**, B04203, doi:10.1029/2005JB003934.

Symonds, R. B., Rose, W.I., Bluth, G. & Gerlach, T. M. (1994). Volcanic gas studies: methods, results, and applications.

Downloaded from http://petrology.oxfordjournals.org/ by guest on March 22, 2015

In: Carroll, M. R. & Holloway, J. R. (eds) *Volatiles in Magmas. Mineralogical Society of America, Reviews in Mineralogy* **30**, 1–66.

Ukawa, M., Fujita, E., Ueda, H., Kumagai, T., Nakajima, H. & Morita, H. (2006). Long-term geodetic measurements of large scale deformation at Iwo-jima caldera, Japan. *Journal of Volcanology and Geothermal Research* **150**, 98–118.

Wallace, P. (2005). Volatiles in subduction zone magmas: concentrations and fluxes based on melt inclusion and volcanic gas data. *Journal of Volcanology and Geothermal Research* **140**, 217–240.

Webster, J. D., Kinzler, R. J. & Mathez, E. A. (1999). Chloride and water solubility in basalt and andesite melts and implication for magmatic degassing. *Geochimica et Cosmochimica Acta* **63**, 729–738.

Yoshimura, S. & Nakamura, M. (2010). Chemical driven growth and resorption of bubbles in a multivolatile magmatic system. *Chemical Geology* **276**, 18–28.

Downloaded from http://petrology.oxfordjournals.org/ by guest on March 22, 2015